Applied Ocean Research 166 (2026) 104902

Contents lists available at ScienceDirect

Applied Ocean Research

journal homepage: www.elsevier.com/locate/apor

Research paper

Landslide impacts on built environment: Numerical analysis of the forces exerted by granular material collapsing on dry and submerged conditions

Gabriel Barajas [a,*], Javier L. Lara [a], Alessandro Romano [b,a], Eduard Puig Montellà [c]

[a] IHCantabria - Instituto de Hidráulica Ambiental de la Universidad de Cantabria, Calle Isabel Torres 15, Santander 39011, Spain
[b] Roma Tre University, Engineering Department, Rome 00146, Italy
[c] Centro Oceanográfico de Canarias. Instituto Español de Oceanografía. Consejo Superior de Investigaciones Científicas (IEO-CSIC), Santa Cruz de Tenerife, 38001, Spain

ARTICLE INFO

Keywords:
CFD
OpenFOAM
Landslide
Granular
Forces

ABSTRACT

Landslide-generated impacts represent a critical hazard for coastal and reservoir infrastructures, yet their underlying fluid dynamics remain poorly understood due to the complexity of turbulent, free-surface flows. In this work, OpenFOAM® is used to investigate sudden impacts on surfaces caused by granular landslides. First, three sets of experiments are used to validate the numerical framework: a dry granular flow impact on a wall in an inclined flume, a debris avalanche impacting a pier and a dam-break interaction of a fluid impact on a vertical cylinder. For each case, numerical predictions are compared with experiments in terms of impact forces, providing confidence that the solver can reproduce sudden loads caused by granular and fluid masses. Then, the validated numerical setup is used to study submerged landslide impacts on slender cylinders, capturing the interaction between the granular slide and the free surface, resolving large-scale vortical structures and their role in energy transfer and dissipation. Results highlight two distinct stages of the phenomenon: (i) the initial impact and jet formation, and (ii) turbulent dissipation and recirculation. The analysis provides quantitative insights into velocity fields, pressure distributions, and turbulence intensities, and identifies key mechanisms driving energy loss. These findings contribute to a deeper physical understanding of landslide–impacts and offer a basis for improved hazard assessment and engineering design of protective structures.

1. Introduction

Landslide impacts on the built environment represent a significant hazard capable of causing severe structural damage. In particular, submarine slides pose a critical threat to offshore infrastructure such as pipelines, platforms, and pile-supported structures, both fully submerged and partially exposed. Ensuring the safety of these facilities has drawn increasing attention in recent years. However, assessing landslide–infrastructure interactions through physical experiments is highly challenging, given their complexity and cost. As a result, the use of computational fluid dynamics (CFD) has become increasingly widespread in both industry and academia, offering a powerful and cost-effective tool to simulate multiple extreme scenarios with high accuracy, while complementing laboratory investigations.

Regarding the impacts on buildings, Luo et al. (2023) reviews the mechanisms of interaction between landslide structures and the classification systems of the damage state of buildings. The interaction between a landslide and a building has been numerically simulated, with a two-dimensional (2D) or three-dimensional (3D) analysis. Luna et al. (2011), with a 2D Eulerian formulation in finite differences, develops physical vulnerability curves for debris flows and determines the zones where elements at risk could suffer an impact. In addition, Cuomo (2021) uses a 2D approach to analyze the dynamic impact of fast moving flow-like landslides against structures such as masonry walls and buildings, using the Material Point Method (MPM) to accurately track the spatial and temporal distribution of stresses in both flow and structure. Luo et al. (2019) uses a 3D approach to evaluate the effect of blockage of buildings on the mobility of landslides and the associated energy dissipation mechanisms.

Submarine pipelines are critical installations on the seafloor used to transport strategic energy and mineral resources from offshore production fields to processing and storage facilities (Kaiser, 2017). Understanding landslide–pipeline interaction is essential to reduce damage and maintenance costs. Prior studies have analyzed impact forces from submarine debris flows on pipelines, separating stable from peak loads and elucidating controlling mechanisms. This studies also report geometry, impact angle, and environmental effects, and include validations

---

* Corresponding author.
E-mail address: barajasg@unican.es (G. Barajas).

https://doi.org/10.1016/j.apor.2025.104902
Received 17 September 2025; Received in revised form 16 December 2025; Accepted 23 December 2025

against experiments (Qian et al., 2023, 2020; Zakeri et al., 2008; Liu et al., 2015; T.-k. et al., 2018). Design-oriented CFD work further explores mitigation, e.g., surface perforation patterns that delay separation and reduce drag, and the influence of pipeline–seabed gaps and diameter on impact forces (Guo et al., 2021; Fan et al., 2022).

However, many simulations idealize structures as fixed boundaries, neglecting structural deformation and true mechanical response under impact, which hinders reliability assessment under extreme conditions (Wang et al., 2024). For example, Wang et al. (2024) report that bucket foundations impacted by offshore landslides experience a force that decreases after the initial peak and then stabilizes.

Similar stiffness-contrast mechanisms arise for pile-supported structures: Martin and Chen (2005) show that relative stiffness between pile and soil governs failure modes and pile loading under translational embankment failures, a consideration also relevant to offshore piles.

In parallel, high-fidelity approaches have been developed for landslide–fluid–structure interaction. Lagrangian particle methods (DEM) capture dry impacts on rigid (Zhang et al., 2020) and flexible barriers (Albaba et al., 2017). In the presence of fluid, the dynamics become more complex due to additional physical processes. To address these complexities, coupled multiphase techniques capable of capturing detailed small-scale physics have been developed, such as coupled Smoothed Particle Hydrodynamics (SPH)– Discrete Element Method (DEM) methods, which have been validated against laboratory-scale experiments (Liu and Liang, 2022; Luo et al., 2022). Fully coupled fluid–granular–structure approaches like CFD–DEM (and extensions such as CFD–DEM–Finite Element Method (FEM)) have also been employed to study debris flows and landslide impacts on rigid (Fang et al., 2022) and flexible barriers (Leonardi et al., 2016; Li and Zhao, 2018). Their main limitation is computational cost, restricting domain size and duration.

An alternative is multiphase Eulerian “two-fluid” modeling, treating fluid and grains as interpenetrating continua with drag coupling and a non-Newtonian granular rheology. These models can capture pore-pressure evolution and span loose to dense regimes (Montellà et al., 2021, 2023), and have been used for landslide-generated tsunamis (Rauter et al., 2022a). Despite a favorable accuracy–cost balance, full-scale applications remain challenging.

For realistic engineering scenarios, where the goal is to capture the main loads exerted by landslides on structures rather than the detailed grain-scale mechanics, a balance between physical accuracy and computational tractability is essential. Fully resolved approaches such as CFD–DEM or Eulerian two-fluid models provide valuable insights into pore-pressure transients, grain–fluid slip, or local contact mechanics, but their prohibitive computational cost limits their applicability to small domains or short time windows. In contrast, continuum formulations allow for larger spatial and temporal scales while retaining the ability to reproduce bulk dynamics of the granular phase. Consequently, in this work we represent the landslide as a single-phase granular continuum embedded in a multiphase (air–water–granule) Volume of Fluid (VOF) framework within OpenFOAM®. This strategy, validated in previous benchmark studies (Romano et al. (2023)), enables us to resolve the dominant momentum transfer from the granular mass to the surrounding fluid and the resulting large-scale vortical structures, which are the key drivers of impact forces on slender cylinders. By adopting this formulation, the model remains computationally efficient yet sufficiently robust to address engineering-scale problems relevant for hazard assessment and offshore infrastructure design.

1.1. Aims of the present article

This paper focuses on the use of OpenFOAM (Jasak, 1996), an open-source C++ toolbox for developing customized numerical solvers and utilities. The versatility of OpenFOAM is evident in its application to landslides, as its ability has been widely reported in the literature and is very useful for modeling in detail the complex phenomena that occur. There are different approaches depending on the type of material, either for rigid material (Romano et al. (2020)) or deformable/granular material (Von Boetticher et al. (2016), Paris et al. (2021), Rauter et al. (2021) Rauter et al. (2022a), Romano et al. (2023), Romano et al. (2025)). To the best of our knowledge, no investigations (experimental or numerical) have yet been published that specifically evaluate the effects of submerged granular landslides on pile-supported structures. This absence in the literature highlights both the complexity of the problem and the need for tractable modeling approaches capable of complementing laboratory experiments. In this context, CFD solvers provide a valuable framework to pre-assess experimental designs and to explore parameter spaces that would be prohibitively expensive to reproduce physically. Therefore, the present work aims to fill this gap by extending the applicability of OpenFOAM® to the study of submerged landslide impacts on slender cylinders. Through a series of numerical simulations, we quantify the maximum forces exerted on the obstacles and examine the underlying mechanisms that govern when and why these forces occur. Due to the relative simplicity of the adopted rheological formulation, the proposed framework enables fast and efficient simulations, making it a practical and complementary tool to physical testing in engineering-scale scenarios.

Since no publicly available studies have evaluated the effects of submerged granular landslides on piles, the present numerical model is validated by isolating key physical processes and comparing them with established benchmarks (e.g., Cui and Jeng (2024) and Renaud et al. (2025)). This stepwise validation strategy demonstrates that the overall uncertainty of such complex phenomena can be reduced by testing and confirming each process separately.

The structure of the manuscript is organized as follows: after the introduction, Section 2 elaborates on the governing equations, and the description of the numerical model framework (i.e. OpenFOAM®) and the rheological model used to simulate the granular landslides is provided. Then, in Section 3, the ability of the numerical model to reproduce sudden impacts of landslides in structures is validated with three sets of experiments: a dry granular flow impact on a wall in an inclined flume, a debris avalanche impacting a pier and a dam-break interaction of a fluid impact on a vertical cylinder. A Reynolds Averaged Navier–Stokes ($RANS$) turbulence model was adopted, as it is the most common model used in the engineering field because of its accuracy and relatively reduced computational costs. Next, in Section 4, a numerical analysis of the forces generated by the sudden impact of submerged granular material on a slender cylinder is carried out. A Large Eddy Simulation (LES) approach is defined to take into account the complex flow structures that are generated and that influence the forces exerted on the obstacles: large structures will be resolved, while small structures will be modeled. This choice of using LES builds on previous research by Li and Fuhrman (2022) that demonstrated that the breaking point and the peak force on a vertical cylinder due to incipient breaking should not be affected by the turbulence closure model. Firstly, the influence of the variation of the radius of the cylinder and, secondly, the shift of its position are analyzed. A comparison of different turbulent modelizations, the analysis of accuracy and computational cost, and the ability to solve large flow structures is presented. Qualitative and quantitative descriptions of the numerical results, in terms of maximum forces and granular displacements during the landslide process, are provided. Finally, a conclusion, Section 5, closes the article.

2. Numerical model

This study builds on the OpenFOAM suite of tools, as previous works Von Boetticher et al. (2016) and Romano et al. (2023), have proven that it is an efficient and accurate tool for modeling rigid or deformable/granular, submerged, or subaerial landslides.

2.1. Governing equations

The implementation of the governing equations in the OpenFOAM framework is described in Romano et al. (2023)

The fluid dynamics in the main domain are governed by the 3D $RANS$ equations, which encompass the conservation of mass and momentum (to model the fluid flows), coupled with the Volume of Fluid (VoF) equation (to model the interface between water, granular material, and air). The $multiPhaseInterFoam$ solver from OpenFOAM-v2312 (ESI-Group (2023)) was utilized in all the simulations of this work, which is designed for transient simulations involving two or more incompressible, isothermal and immiscible fluids. These equations are represented as follows:

$$\frac{\partial u_i}{\partial x_i} = 0 \tag{1}$$

$$\frac{\partial(\rho u_i)}{\partial t} + \frac{(\partial \rho u_i u_j)}{\partial x_j} = -g_j x_j \frac{\partial \rho}{\partial x_i} - \frac{\partial p^*}{\partial x_i} + \frac{\partial \tau_{ij}}{\partial x_j} + f_{\sigma i} \tag{2}$$

$$\frac{\partial \alpha}{\partial t} + \frac{(\partial u_i \alpha)}{\partial x_i} + \frac{\partial(u_{ci}\alpha(1-\alpha))}{\partial x_i} = 0 \tag{3}$$

where u_i are the ensemble averaged components of the velocity, x_i the Cartesian coordinates, g_j the components of the gravitational acceleration, ρ the density of the fluid, p^* the ensemble averaged pressure in excess of hydrostatic, α the volume fraction (VoF), $f_{\sigma i}$ the surface tension, u_{ci} is the compression velocity and τ_{ij} the shear stress. For the fluid phases (water and air) we assume a Newtonian closure:

$$\tau_{ij} = 2\mu_{\text{eff}} S_{ij} - \frac{2}{3}\mu_{\text{eff}} \frac{\partial u_k}{\partial x_k}\delta_{ij} \tag{4}$$

where μ_{eff} is the effective dynamic viscosity that is defined as $\mu_{\text{eff}} = \mu + \rho\nu_t$ and takes into account the dynamic molecular (μ) and the turbulent viscosity effects ($\rho\nu_t$). Finally, S_{ij} is the strain rate tensor.

$$S_{ij} = \frac{1}{2}\left(\frac{\partial u_i}{\partial x_j} + \frac{\partial u_j}{\partial x_i}\right) \tag{5}$$

The granular phase, on the contrary, does not behave as a Newtonian fluid, so a different constitutive relation between the shear stress and the deformation is required. Previous studies have used a variety of rheologies to capture the complex behavior of debris flows, landslides, and avalanches, including Bingham Gauer et al. (2006), Herschel–Bulkley Ren et al. (2019), Coulomb-viscoplastic laws (e.g. Domnik and Pudasaini, as used in Romano et al. (2023)), and the $\mu(I)$ rheology Rauter (2021), among others.

2.2. Rheology model

In this work, for cases involving water–slide interaction, we use the non-Newtonian Coulomb viscoplastic rheological model based on the work of Romano et al. (2023). In addition, the present article also incorporates the $\mu(I)$ rheology to describe dry, dense granular flows with rate-dependent frictional behavior. Both models are applied to a dry granular collapse in an inclined plane to compare their performance in a friction-dominated regime, while the remaining test cases use the Coulomb-viscoplastic model.

2.2.1. Non-Newtonian Coulomb viscoplastic rheology

The non-Newtonian Coulomb viscoplastic rheological model is used to model the behavior of the deformable granular material, which is implemented in the standard solver $multiPhaseInterFoam$ ESI-Group (2023). This rheology was originally implemented and validated in OpenFOAM® by Von Boetticher et al. (2016) to analyze debris flows that occur in the air.

In this case, the shear stress tensor is computed as follows:

$$\tau_{ij} = 2\mu_s S_{ij} \tag{6}$$

Following Domnik and Pudasaini (2012), the dynamic viscosity μ_s is modeled as follows:

$$\mu_s = \mu_{min} + \frac{p\sin(\delta)}{\|\mathbf{S}\|}\left(1 - \exp^{-m_y\|\mathbf{S}\|}\right). \tag{7}$$

m_y is a numerical parameter, p is the pressure, δ the internal friction angle of the granular material, μ_{min} is a minimal dynamic viscosity, and $\|\mathbf{S}\|$ is the norm of the strain rate tensor S_{ij} defined by Domnik and Pudasaini (2012) as:

$$\|\mathbf{S}\| = \sqrt{2S_{ij}S_{ij}}, \tag{8}$$

The strength of this numerical approach lies in its simplicity, flexibility, and computational efficiency, relying on only a few physically based parameters. In the present single-phase VOF framework, the Coulomb-viscoplastic yield law uses the pressure field and does not resolve pore-pressure dynamics. This modeling choice has been widely adopted in similar continuum approaches and has proven suitable for wet granular flows such as debris flows, mudflows, and mixed landslides Von Boetticher et al. (2016), Romano et al. (2023)

2.2.2. $\mu(I)$ rheology

The $\mu(I)$ rheology assumes that the solid-phase shear stress $\boldsymbol{\tau}$ is proportional to the solid pressure p, following a frictional law dependent on the inertial number I (Da Cruz et al., 2005):

$$\tau_{ij} = \mu(I)p\frac{S_{ij}}{\|\mathbf{S}\|}, \tag{9}$$

where $\mu(I)$ is the friction coefficient depending on the inertial number I. The inertial number I quantifies the ratio of the macroscopic deformation timescale to the microscopic rearrangement timescale and is defined as:

$$I = \frac{d\|\mathbf{S}\|}{\sqrt{p/\rho_s}}, \tag{10}$$

where d is the particle diameter and ρ_s is the solid density. To relate the friction coefficient to the inertial number, Jop et al. (2005) proposed the following empirical relation:

$$\mu(I) = \mu_1 + \frac{\Delta\mu}{I_0/I + 1}, \tag{11}$$

where μ_1 is the static friction coefficient, $\Delta\mu$ is the difference between dynamic and static friction, and I_0 is a reference inertial number. This model is more suitable for modeling dry, dense granular flows such as chute flows, silo flows, or avalanches Jop et al. (2005). In this study, the $\mu(I)$ rheology is applied only to the dry benchmark comparison in Section 3.1 because the present single-phase VOF model does not resolve pore-pressure dynamics, which would affect the pressure-dependent response of $\mu(I)$ in saturated or submerged conditions.

2.3. Turbulence model

Turbulence is a very complex phenomenon with a wide spectrum of scales of fluid motion. Large- and small-scale motions have different features, as stated by Schumann (1996). Turbulence is governed by the same basic equations as general laminar flows adding the turbulent fluctuating motions.

Turbulent flows are characterized by eddies with a wide range of lengths and time scales. The largest eddies are typically comparable in size to the characteristic length of the mean flow. The smallest scales are responsible for the dissipation of turbulence kinetic energy.

In order to determine which turbulence modeling approach is the most adequate when simulating complex fluid flows, it is necessary to characterize the different methods that have been suggested in the literature. Following Rodi et al. (2013), these equations can be solved numerically and three major families can found: (i) Direct Numerical Simulations (DNS), which does not introduce any numerical modelization so all scales of the turbulent motion, ranging from large to small are resolved, (ii) $RANS$, in which the turbulent fluctuations are averaged out and only equations governing mean-flow quantities are solved and (iii) LES, which is between DNS and $RANS$, solving turbulent flow equations for large scales and modeling the motions of small scales.

There is a hybrid $RANS$-LES approach named Detached Eddy Simulation (DES), which is a modification of a $RANS$ turbulence model where the model switches to a sub-grid scale formulation in regions fine enough for LES calculations.

As DNS turbulence models need very detailed meshes with cell sizes that must be smaller than the smallest dissipative eddies, this method is not suitable for most research or consultancy projects because of the high computational resources and times needed. However, because the $RANS$ turbulence model approach does not solve the eddies, the cell size can be enlarged and therefore the simulation costs and times are much more effective, making it highly recommended for general CFD simulations. However, because of the development of High-Performance Computing (HPC) clusters and relatively affordable access to advanced computational resources, LES is becoming more popular for solving turbulent flows when large structures become relevant, replacing $RANS$ approaches.

It is stated by Ekat et al. (2023), and is well known that the $RANS$ models are less accurate than the LES models in predicting secondary flow. Although pure LES is feasible for large computational domains and high Reynolds numbers, it requires high computational costs. To optimize computational cost and accuracy, hybrid $LES/RANS$ models can be used. They combine $RANS$ in the wall region and LES in the core flow.

Viscous effects near walls are characterized by the non-dimensional wall distance:

$$y^{+} = \frac{u^{*} y}{\nu} \tag{12}$$

where u^{*} is the friction velocity, y is the distance to the wall, and ν is the kinematic viscosity of the fluid. LES, $RANS$, and DES wall functions are valid throughout the boundary layer and for values of y^{+} < 300.

2.3.1. LES turbulence models

LES turbulence models only resolve the large scales in the flow, filtering, or eliminating the small scales, which reduces the computational costs considerably compared to DNS turbulence models. The mean flow and the large-scale structures with a length scale larger than the filter size (often taken as the grid size) are resolved, and the small-scale turbulence is modeled using a subgrid-scale model. There are several models to approximate the apparent stress tensor introduced into the governing equations, or the sub-grid scale stress tensor, such as Algebraic Dynamic model, Dynamic subgrid-scale model ($DSGS$), Wall-adapting local eddy-viscosity (WALE) or Smagorinsky–Lilly, among others.

In the present work, the Smagorinsky turbulence model is chosen, Smagorinsky (1963), which is based on the assumption that the Reynolds number is sufficiently high to ensure that energy is transferred from large to small scales, which are responsible for dissipation only and do not transfer any energy. Small scales are eliminated by filtering the turbulence field, that is, applying a filter (i.e., Top-Hat filter, Cut-Off filter or Gauss Filter) to the Navier–Stokes equations, resulting in the filtered continuity equation:

$$\frac{\partial [u_i]}{\partial x_i} = 0 \tag{13}$$

and the filtered momentum equation:

$$\frac{\partial [u_i]}{\partial t} + \frac{\partial [u_j][u_i]}{\partial x_j} = -\frac{1}{\rho}\frac{\partial p}{\partial x_i} + \frac{\partial}{\partial x_j}\nu\left(\frac{\partial [u_i]}{\partial x_j} + \frac{\partial [u_j]}{\partial x_i}\right) + \frac{1}{\rho}\frac{\partial \tau_{sgs}}{\partial x_i} \tag{14}$$

where u_i is the filtered velocity of the fluid, $x_{i,j}$ is the Cartesian coordinates, ρ is the density, p is the pressure and ν is the kinematic viscosity. The sub-grid stresses τ_{sgs} expresses how the filtered micro-estructure exerts an effective stress to the large eddies and is defined as:

$$\tau_{sgs} = K_s\left(\frac{\partial [u_i]}{\partial x_j} + \frac{\partial [u_j]}{\partial x_i}\right) \tag{15}$$

where K_s is the sub-grid eddy viscosity defined as:

$$K_s = L^2\left|\frac{\partial [u_i]}{\partial x_j} + \frac{\partial [u_j]}{\partial x_i}\right| \tag{16}$$

and L is the mixing length, which can be expressed by means of the constant C_s and the characteristic grid distance Δ as follows:

$$L = C_s \Delta \tag{17}$$

2.3.2. RANS turbulence models

$RANS$ turbulence models resolve the mean flow, but the effects of turbulence fluctuations on the mean flow are modeled using a turbulence model. As for LES models, in $RANS$ there are many different models, such as $k-\epsilon$, Realizable $k-\epsilon$, RNG $k-\epsilon$, Spalart–Allmaras or $k-\omega$ Shear Stress Transport (SST), among others.

In the present work, the k–ω-SST turbulence model, Menter (1993), is chosen, which has become very popular for general CFD applications. It is a hybrid model that combines the Wilcox $k-\omega$ turbulence model Wilcox (1988) and the $k-\epsilon$ turbulence model Launder and Sharma (1974). A blending function activates the $k-\omega$ turbulence model near the wall and the $k-\epsilon$ turbulence model in the free stream. The k-ω-SST model from Larsen and Fuhrman (2018) has been used for turbulence modeling because it provides a stable solution for overproduction of turbulence levels beneath waves.

The turbulence kinetic energy κ is given by:

$$\frac{\partial \rho\kappa}{\partial t} + u_j\frac{\partial \rho\kappa}{\partial x_j} = \rho P_k - \rho P_b - \rho\beta^{*}\kappa\omega + \frac{\partial}{\partial x_j}\left[\left(\mu + \rho\sigma^{*}\frac{\kappa}{\omega}\right)\frac{\partial \kappa}{\partial x_j}\right] \tag{18}$$

and the turbulence specific dissipation rate ω equation is given by:

$$\frac{\partial \rho\omega}{\partial t} + u_j\frac{\partial \rho\omega}{\partial x_j} = \rho P_\omega - \rho\beta\omega^2 + \rho\frac{\sigma_d}{\omega}\frac{\partial \kappa}{\partial x_j}\frac{\partial \omega}{\partial x_j} + \frac{\partial}{\partial x_j}\left[\left(\mu + \rho\sigma\frac{\kappa}{\omega}\right)\frac{\partial \omega}{\partial x_j}\right] \tag{19}$$

where u_j is the velocity of the fluid, μ is the dynamic viscosity and ρ the density of the fluid. P_k is the shear production, P_b is the buoyancy production. Other model coefficients are α_{k1}, α_{k2}, α_{w1}, α_{w2}, β_1, β_2, β^{*}, γ_1, γ_2, a_1, b_1 and c_1.

As described in Larsen and Fuhrman (2018), the eddy viscosity ν_t is:

$$\nu_t = \frac{a_1\kappa}{max\left(a_1\omega, F_2\sqrt{p_0}, a_1\lambda_2\frac{\beta}{\beta^{*}\alpha}\frac{p_0}{p_\Omega}\omega\right)} \tag{20}$$

where a_1, λ_2, β, β^{*} and α are model coefficients, F_2 is a blending function, p_0 the turbulence production term and p_Ω the rotation correction term.

2.3.3. DES turbulence models

DES turbulence model is a hybrid approach in which a $RANS$ approach is used for regions near solid boundaries and where the turbulent length scale is less than the maximum grid dimension and switches to a LES approach when the turbulent length scale exceeds the grid dimension. Again, there are many different models, such as $\kappa-\omega$-SST Delayed Detached Eddy Simulation ($DDES$), $\kappa-\omega$-SST Improved Delayed Detached Eddy Simulation (IDDES) or Spalart–Allmaras Delayed Detached Eddy Simulation ($DDES$).

In the present work, the Spalart–Allmara-$DDES$ turbulence model is chosen Spalart et al. (2012), as it is a cost effective procedure that treats the largest eddies through a conventional LES, while handling the boundary layers and thin shear layers with the conventional $RANS$ approach (Wilcox, 2006).

The transport equation for the eddy viscosity ν_t is given by:

$$\frac{\partial \bar{\nu}}{\partial t} + \frac{\partial \rho u_j \bar{\nu}}{\partial x_j} - \frac{1}{\sigma}\left[\frac{1}{\partial x_j}\left(\rho(\nu+\bar{\nu})\frac{\partial \bar{\nu}}{\partial x_j}\right) + C_{b2}\rho\frac{\partial \bar{\nu}}{\partial x_i}\frac{\partial \bar{\nu}}{\partial x_i}\right] = C_{b1}\rho S\bar{\nu}(1-f_{t2}) - \rho\left(C_{w1}f_w - \frac{C_{b1}}{\kappa^2}f_{t2}\right)\frac{\bar{\nu}}{\bar{d}}^2 \tag{21}$$

The length scale d is defined by:

$$\bar{d} = min(d, C_{DES}\Delta, y) \tag{22}$$

where $\bar{\nu}$ is the viscosity-like variable, u_j is the velocity of the fluid. Δ is the chosen measure of grid spacing and C_{DES} is a calibration constant. Other model coefficients are k, $\sigma_{\mu t}$, C_{b1}, C_{b2}, C_{w1}, C_{w2}, C_{w3}, C_{v1}, C_s, C_{DES}, C_k, C_{t3}, C_{t4} and f_w^*.

As stated in Pope (2000), LES simulations with near-wall modeling ($LES - NWM$), in which the filter and grid are too coarse to resolve the near-wall motions so that their influence is modeled explicitly or implicitly, are sufficiently fine to resolve 80% of the energy remote from the wall. Substantial computational savings accrue if the viscous wall region is not resolved. The quality of the LES simulations are measured with the fraction of turbulent kinetic energy M(x,t) in the resolved motions Pope (2000) as:

$$M(x,t) = \frac{\kappa_r(x,t)}{K(x,t)+\kappa_r(x,t)} \tag{23}$$

which requires the determination (locally in space and time) of the turbulent kinetic energy of the resolved motions, with

$$K(x,t) = \frac{1}{2}\langle(W - \langle W\rangle) * (W - \langle W\rangle)\rangle \tag{24}$$

namely, the resolved velocity field W(x, t) and the residual motions $\kappa_r(x,t)$. Thus, the value of M is between 0 and 1: $M = 0$ corresponds to DNS and $M = 1$ to $RANS$. The lower values of M correspond to the resolution of more of the turbulent motions.

3. Validation of the numerical framework against benchmark cases

Non-Newtonian Coulomb viscoplastic rheology, implemented in OpenFOAM, has been shown to reproduce both laboratory-scale and large-scale debris flow experiments with good agreement in terms of runout distances, impact forces, and generated waves, while significantly reducing computational cost compared to multiphase drag-based models. This single-phase continuum approach incorporates pressure- and shear-rate-dependent behavior, allowing the simulation of complex 3D flow structures and their interaction with obstacles. Validation studies (e.g., Viroulet et al. (2014); Mohammed and Fritz (2012); Grilli et al. (2017); Romano et al. (2020)) demonstrate that the method reliably captures granular kinematics and force magnitudes, as well as fluid response and wave characteristics, confirming that the momentum transfer between phases is well reproduced. In dry configurations, this reduces mainly to predicting front evolution and impact loads on obstacles, while in submerged conditions additional pore-pressure effects occur. Since the model does not explicitly resolve volume-fraction evolution or transient pore pressures, mechanisms such as hydroplaning, excess pore pressure, fluid–solid slip, or shear-band thickness are only approximated through an effective viscosity. More advanced models, such as Eulerian two-fluid approaches (Montellà et al. (2023); Rauter et al. (2022a)) or grain-resolved CFD–DEM Fan et al. (2022), can capture pore-pressure transients, dilatancy, and contact mechanics, but at prohibitive computational cost for engineering scales.

For this reason, we adopt the single-phase formulation as a practical compromise: it is fast and robust, able to capture bulk dynamics and global loads with sufficient accuracy, and thus suitable for addressing the nonlinear impact processes of submerged granular landslides on slender cylinders.

To the authors' knowledge, no previous numerical studies have directly addressed this specific problem, which underscores both the novelty and the relevance of the present work.

OpenFOAM® has been shown to reproduce both submerged and aerial granular landslides Romano et al. (2023), but there is still limited evidence of its accuracy in predicting forces from sudden impacts of submerged granular flows. To reduce this uncertainty, the framework is validated by isolating key processes following the approach of Cui and Jeng (2024) and Renaud et al. (2025).

Three benchmark cases are simulated with multiPhaseInterFoam (Section 2), defining two phases with identical properties to mimic dry granular slides or fluid dam-breaks. The first (Section 3.1) is a quasi-2D dry granular slide impacting a wall, used to test the force evolution during sudden impacts. The second (Section 3.2) is a 3D granular slide striking a bridge pier, which evaluates the solver's ability to capture complex impacts on slender obstacles. The third (Section 3.3) is a 3D dam-break impacting a vertical cylinder, extending the validation to fluid-driven forces. In each case, numerical predictions are compared with experiments in terms of impact forces, providing confidence that the solver can reproduce sudden loads caused by granular and fluid masses. These validations confirm OpenFOAM as a reliable and efficient tool for modeling extreme impact processes.

3.1. Dry granular landslide impact on an inclined flume

As described in Jiang and Towhata (2013), the impact of dry granular flow against a rigid retaining wall is analyzed to measure the total normal force acting on the affected structure.

A series of physical model experiments were carried out in an inclined flume ($\phi = 40°$), which measured 2.93 m in length, 0.35 m in height and 0.3 m in width. The length and width of the initial deposition of the sliding mass are 0.44 m and 0.3 m, respectively. The height of the initial deposition (H[m]) is set to 0.15 m.

Appendix A presents the grid analysis to select a numerical discretization that combines accuracy and speed in the simulations. The numerical tank (NT) is 2.93 m long, 0.35 m wide and 0.3 m high, and is characterized by a cell resolution of 0.005 m along the x direction, 0.3 m along the y direction (2D, one cell only), and 0.005 m along the z direction. The computational domain is discretized into a structured grid and contains 0.04M cells.

The four side walls are defined as slip boundaries, the top as an open boundary, while the bottom wall is set to partialSlip because in granular materials, particles can roll and slide above the inclined plane. In the present work, MULES is used to solve the VoF equation and the PIMPLE algorithm to solve the velocity–pressure coupling in the fundamental equation. For the granular material rheological model, the following parameter values have been used: $m_y = 0.1$ s, $\delta = 53°$ and $\mu_{min} = 5\ Pa\ s$. $multiPhaseInterFoam$ is used to simulate the case, with two phases defined as air. The $\kappa\omega - SST$ turbulence model has been selected.

To test the model's ability to reproduce the experimentally observed frictional behavior of granular flows, particularly during rapid impacts, we also consider the $\mu(I)$ rheology alongside the Non-Newtonian Coulomb viscoplastic model (Domnik and Pudasaini, 2012). The $\mu(I)$ rheology, described in Section 2.2.2, has been shown to effectively capture the rate-dependent behavior of dense granular materials (Fall et al., 2015; Chauchat et al., 2017). Although the viscoplastic model used here includes the rate dependence, it does not explicitly account for the evolution of internal friction as a function of the granular flow regime. In contrast, the $\mu(I)$ rheology captures this evolution through the inertial number, making it more suitable for describing shear-localized, impact-driven flows. This comparison between rheological models helps assess the validity of the Non-Newtonian Coulomb viscoplastic approach in capturing the key dynamics of dense granular flows.

The evolution of the wall force is shown in Fig. 1. For the Non-Newtonian Coulomb viscoplastic model, a *partialSlip* value of 0.008 yields the best match to the experimental peak. For the $\mu(I)$ model, 0.005 results in a more accurate peak magnitude and timing. The force

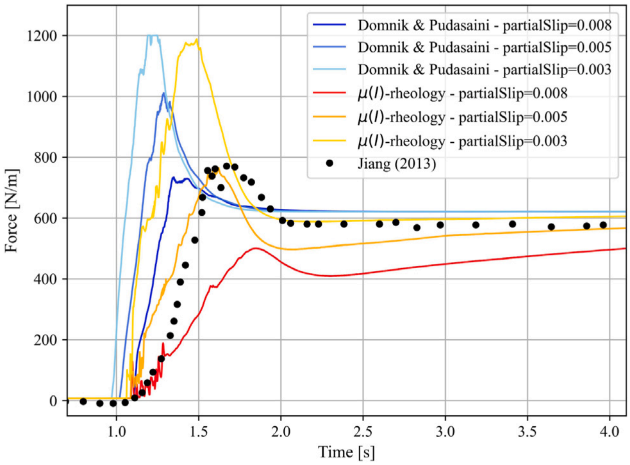

Fig. 1. Force evolution for debris avalanche that impacts a rigid barrier. Different bottom boundary conditions are tested for both Non-Newtonian Coulomb viscoplastic and the $\mu(I)$ rheologies. The experimental data from Jiang and Towhata (2013) is displayed in black dots.

overshoot becomes less pronounced for larger *partialSlip* values which tend towards the no-slip boundary conditions are applied. The $\mu(I)$-rheology better captures the dynamic surge due to its rate-dependent friction, whereas the Non-Newtonian Coulomb viscoplastic model better captures the long-term residual force. This highlights the importance of both rheology and basal boundary condition calibration in realistic simulations.

Fig. 2*a* shows the final deposit shape for both the Non-Newtonian Coulomb viscoplastic model and the $\mu(I)$-rheology. Both reproduce the accumulation area behind the barrier reasonably well, yet important differences are observed. In the $\mu(I)$ case, the upper part of the deposit exhibits a rounded top, similar to that reported in the experiments, suggesting a good representation of surface curvature due to internal frictional resistance. However, the shape diverges from the experimental profile at the tail, which appears to be overly elongated, possibly due to continued creeping motion driven by residual shear. In contrast, the Non-Newtonian Coulomb viscoplastic model produces a more triangular deposit shape similar to a fluid-like response, where yielding is governed by a threshold criterion. Figs. 2*b* and *c* show the velocity field right after the force peak. These velocity maps evidence the stagnant region, or dead zone, characterized by very low velocities. As the flow decelerates, the dead zone near the wall grows progressively. In the end, this region contains most of the deposited material. At that stage, the weight of the dead zone accounts for the residual static force measured on the wall, indicating that the dynamic impact has transitioned into a steady load governed by the final deposit (see Fig. 1). Both models predict a dead zone, but with distinct features. The viscoplastic model forms a clear wedge of near-zero velocity while the granular material flows above (see Fig. 2*b*). The velocity field obtained from $\mu(I)$ model is illustrated in Fig. 2*c*. The $\mu(I)$ model, while physically more representative of granular friction, results in a more diffuse transition and slight residual motion within the dead zone, a consequence of its continuous stress–strain-rate formulation without a strict yield cutoff. This distinction is not merely geometric, it directly relates to the forces on the wall. The dynamic impact phase, associated with a sharp overshoot in the force signal (see Fig. 1), corresponds to the inertial momentum transfer as the material hits the wall. The subsequent plateau is governed by the static load transmitted through the dead zone, which depends on how well the rheology captures the transition from motion to rest. Thus, the shape of the final deposit, especially the geometry and extent of the dead zone, directly influences both the magnitude and evolution of the forces exerted on structures during granular impacts.

Concerning the morphological evolution of the granular phase, Fig. 3 shows the time evolution of the landslide modeled using the Non-Newtonian Coulomb viscoplastic rheology. Fig. 3*a* ($t = 0.0$ s) shows the initial configuration of the granular material before being released. In Fig. 3*b*, the material begins to flow downslope under gravity. As shown in Fig. 3*c*, the granular material continues to slide and stretch along the inclined plane before impacting the wall. In Fig. 3*d*, material accumulates in the lower part of the domain. Most of it becomes stationary, forming a dead zone, while the upper portion continues to flow and deposits on top of the accumulation area. Finally, in Fig. 3*e*, the entire mass comes to rest, forming a triangular-shaped deposit at the base of the slope, consistent with expectations.

Fig. 4 shows the variation of the force evolution when the numerical parameter m_y is varied [0.01, 0.1, 1] s.

Reducing the value of m_y in the viscoplastic rheology (Eq. (7)) makes the material behave more like a Newtonian fluid, with a nearly constant low viscosity. As a result, the granular flow becomes more mobile, producing larger peak forces upon impact and a steeper accumulation front, as illustrated in Fig. 4. Damped oscillations also emerge, likely as a result of the reduced internal resistance during deceleration. In contrast, increasing m_y enhances the rate sensitivity of the rheology, effectively introducing a yield-like behavior. This suppresses the force peak and results in a more gradual and smoother deposition of material at the base of the tank.

Fig. 5 shows the sensitivity to $\mu_{\min}$. In (7), $\mu_{\min}$ acts as a lower bound on the apparent viscosity (a Bingham-like regularization). Over the tested range, the response is only weakly sensitive to $\mu_{\min}$, which indicates that resistance is dominated by $p \sin\delta/\|\mathbf{S}\|$ and that peak forces and the final deposit are controlled mainly by frictional stresses rather than the baseline viscosity.

The two rheological formulations differ in their ability to reproduce key aspects of the flow, ranging from impact dynamics to the geometry of the final deposit. The μ(I) rheology provides a more accurate description of transient forces and unsteady loading, due to its explicit dependence on the shear rate and pressure, which enhances the prediction of impact peaks. In contrast, the viscoplastic Coulomb model offers a better representation of stagnant zones, runout cessation, and the morphology of the deposited material. These complementary behaviors highlight that no single rheology is universally superior. Rather, the choice should be guided by the primary objectives of the simulation, whether the focus is on predicting dynamic impact forces or on capturing the long-term deposition patterns of the landslide.

The maximum y^+ values around the ramp and the wall are less than 30 for the two simulations. The average computational cost was ∼64 core-hours per simulation, taking 8 h days in 8 cores.

3.2. *Dry granular landslide impact on a bridge pier*

As described in Zhong et al. (2022), the impacting process of the debris avalanche against a bridge pier was analyzed. The pier has a height of 10.0 m and a diameter of 1.8 m. The NT of the debris avalanche colliding with the bridge pier has a slope of 60 degrees, the height of the mass center of debris avalanche particles and the dry density are set to be 50.0 m and 1750 kg/m3, respectively. The initial accumulation body of debris avalanches on the slope is a cuboid with a height of 1.0 m, its length and width are 3.0 m and 6.0 m, and the slope surface is considered smooth.

The NT is 40 m long, 6 m wide, and 20 m high, with the same cell discretization presented in Section 3.1, so the grid contains 3.3M cells. The left patch is defined as a no-slip boundary, and open boundary condition has been set at the right patch of the domain. Walls are defined as slip boundaries, the bottom, ramp and cylinder as a non-slip boundary, and the top as an open boundary. The $\kappa\omega - SST$ turbulence model has been selected. For the granular material rheological model, the following parameter values have been used: $m_y = 0.02$ s, $\delta = 34.0$ o

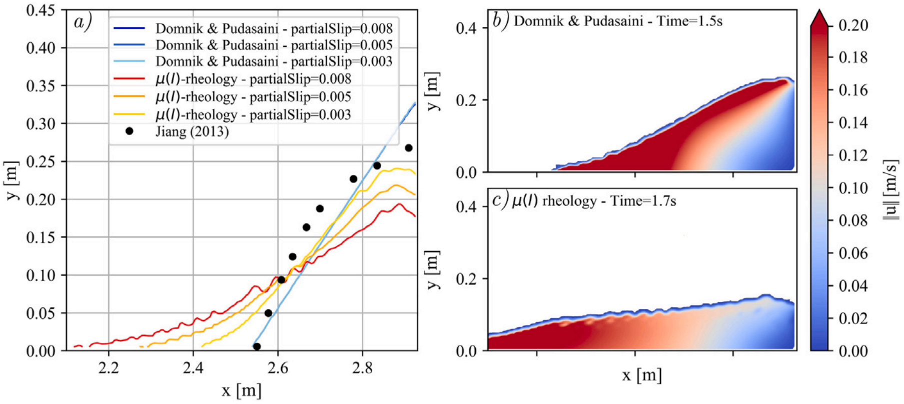

Fig. 2. (*a*) Final deposit shape. Different bottom boundary conditions are tested for both Non-Newtonian Coulomb viscoplastic and the $\mu(I)$ rheologies. The experimental data from Jiang and Towhata (2013) is displayed in black dots. (*b*) Non-Newtonian Coulomb viscoplastic and (*c*) $\mu(I)$-rheology velocity fields within the granular phase right before the force peak.

and μ_{min} = 1e-6 m2/s. Again, $multiPhaseInterFoam$ is used to simulate the case, with two-phases being defined as air.

The impact force between the numerical simulation of Zhong et al. (2022) and the present work is plotted in Fig. 6. The instant of impact of the avalanche is well reproduced, as is the instant of maximum force. However, the maximum numerical force of the impact is found to be underestimated. The experimental maximum force is F_{max} = 0.72 MN in t_{max} = 4.24 s, while the numerical results of the present work are F_{max} = 0.48 MN. Due to the complexity of the 3D case and the simplicity in the modelization of the granular material, the results are in accordance with the previous results.

Fig. 7 shows the evolution of a debris avalanche that impacts a bridge pie. The first image, t = 0.50 s, shows the beginning of the landslide, triggered by gravity. Then, the granular material slides through the inclined ramp (t = 2.00 s). In image t = 4.00 s and t = 4.35 s, the impact and accumulation of material is observed in the windward direction of the bridge pier. The material moves after the bridge due to the high celerity induced in the ramp by gravity.

The maximum $y*+$ values around the ramp and the cylinder are less than 30 for the two simulations. The numerical mesh (3.3M cells) is partitioned to run in parallel in 16 processors, taking 3 days to numerically simulate 5.0 s.

3.3. Fluid dam-break impact on a vertical cylinder

As described in Kamra et al. (2019), the impact of the dam break on a vertical cylinder placed on a dry horizontal bed is performed numerically. Physical experiments were carried out with water in an open reservoir. Therefore, the CFD modeling involves two fluid phases, water and air, and will be modeled with two different numerical approaches. Firstly, the $interFoam$ solver was utilized for the multiphase simulation, which considers the 3D $RANS$ equations for two incompressible fluid phases (water and air) using a Volume of Fluid (VoF) interface capturing approach based on phase fraction. Secondly, the $multiPhaseInterFoam$ solver was utilized, which is designed for transient simulations involving two or more incompressible (water and air, or water, air and granular material), isothermal and immiscible fluids. In order to compare both numerical solvers, water is defined with density ρ = 1000 kg/m3 and kinematic viscosity μ = 1.48e−5 m2/s, air is defined with density ρ = 1 kg/m3 and kinematic viscosity μ = 1e−06 m2/s and the granular material with density ρ = 1 kg/m3 and kinematic viscosity μ = 1e−06 m2/s, so it does behave as air in this simulation involving two fluids. For the granular material rheological model, as $my = 0$, the viscosity model becomes the standard Newtonian rheology that represents fluids such as water and air. Again, $multiPhaseInterFoam$ is used to simulate the case, with two-phases being defined as air.

The NT is 0.8 m long, 0.2 m wide, and 0.6 m high, with a cylinder of diameter of 0.050 m, the center of which is 0.6 m from the left side wall. The height of the water column used is H_c = 0.2 m. The sensor is mounted on the cylinder's left vertical wall (z = 0.011 m). The left patch is defined as a no-slip boundary, and absorption (shallow water active absorption boundary) has been set at the right patch of the domain. Walls are defined as slip boundaries, the bottom, ramp and cylinder as a non-slip boundary, and the top as an open boundary. The $\kappa\omega - SST$ turbulence model has been selected.

Appendix B presents the grid analysis to select a numerical discretization that combines accuracy and speed in the simulations. The NT is characterized by a cell resolution of 0.006 m along the x direction, 0.006 m along the y direction, and 0.008 m along the z direction. The computational domain is discretized into a structured grid and contains 2.6M cells.

The pressure impulse on the vertical wall downstream of the cylindrical obstacle is plotted in Fig. 8, which presents the confirmation that OpenFOAM solvers ($interFoam$ and $multiPhaseInterFoam$) can accurately reproduce an impact on a vertical cylinder. It can be seen that there is good agreement between the experimental data (black circles) and the numerical data $interFoam$ (blue continuous line) and $multiPhaseInterFoam$ (red continuous line). The peak force is well captured either in magnitude or in time. Fig. 9 presents the interaction of the granular material with the cylinder for three different time steps: before impact (t = 0.25 s.), impact(t = 0.35 s.) and after impact (t = 0.50 s).

The maximum y^+ values around the ramp and the cylinder are less than 30 for the two simulations. Both numerical meshes (2.6M cells) were partitioned to run in parallel in 8 processors, taking 1 day to numerically simulate 0.5 s for the solver $interFoam$, and 2.5 days to numerically simulate 0.5 s for the solver $multiPhaseInterFoam$.

4. Application of non-Newtonian Coulomb viscoplastic rheological model to impacts on slender cylinders

Following the work by Romano et al. (2023) in which a numerical wave tank (NWT) in OpenFOAM has been shown to accurately reproduce the granular landslide with a non-Newtonian approach, and

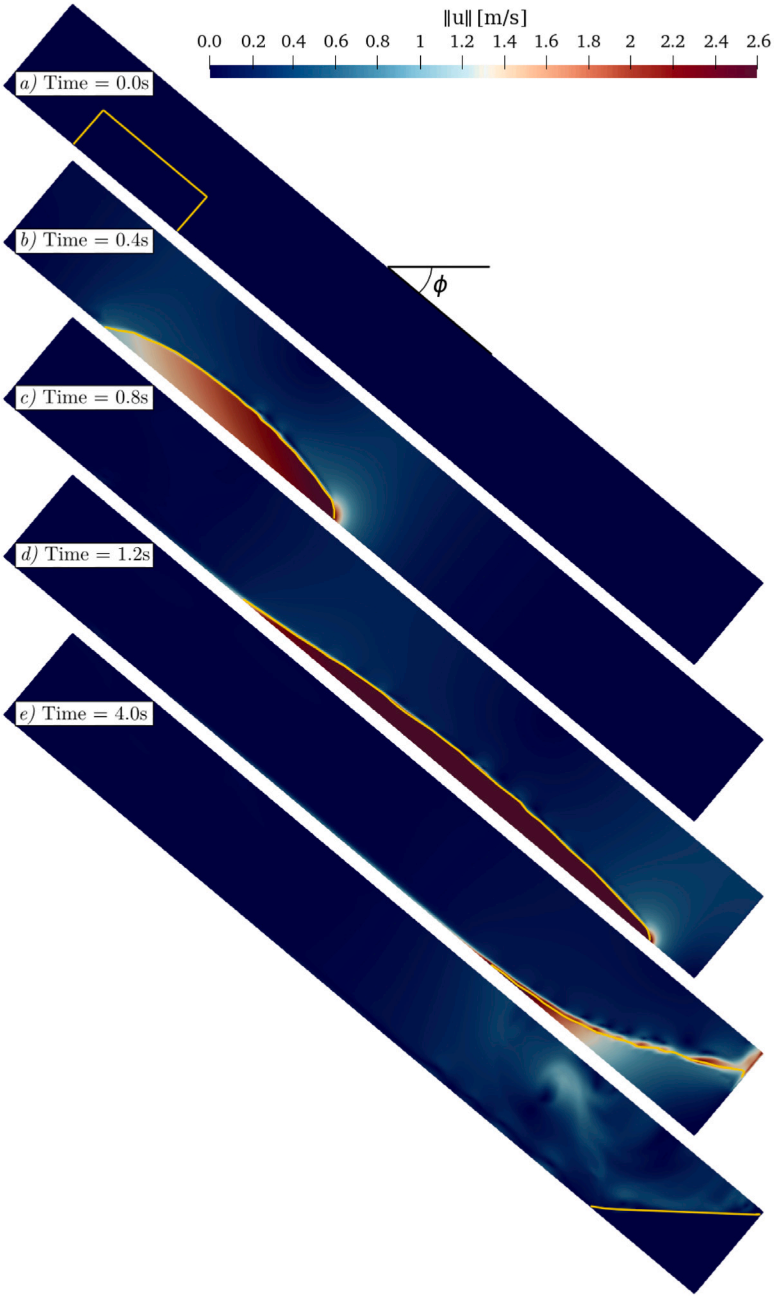

Fig. 3. 2D view of the impact of the granular material in a wall on a incline surface (H = 0.15 m), as described in Jiang and Towhata (2013). Velocity magnitude plotted over the interface material–air (VOF-debris=0.5). Times t = [0.0, 0.4, 0.8, 1.2, 4.0]s., respectively.

Section 3 in which a NWT in OpenFOAM is able to reproduce the impacts of landslides on inclined surfaces and against cylinders, the primary objective of the present work is to extend the use of the applicability of the OpenFOAM and to present numerical investigations of the forces exerted by a granular landslide near the shore in slender cylinders, quantifying the maximum forces, and analyzing why and when they occur.

Focusing on turbulence-modeling approaches, $RANS$ closures remain the most common option in engineering applications because they provide a robust balance between accuracy and computational cost. Within $RANS$, the $\kappa\omega - SST$ model is widely used in wave and fluid–structure interaction problems because it offers improved performance for wall-bounded flows, strong shear layers, and adverse pressure gradients with possible flow separation, while maintaining stable behavior in the outer flow through its blending strategy (Menter (1993); Wilcox (1988)). Consistent with this practice, the $\kappa\omega - SST$ model has been adopted by Romano et al. (2023) for landslide-generated tsunamis, by Di Paolo et al. (2021a) for complex wave propagation, and by Di Paolo et al. (2021b) for wave–structure interaction. However, more advanced approaches such as LES can provide higher fidelity by resolving the large, energy-containing turbulent structures, at the expense of a substantially higher computational cost compared to $RANS$. After validating the numerical wave tank for each process separately in Section 3 using a $RANS$ turbulence closure, the

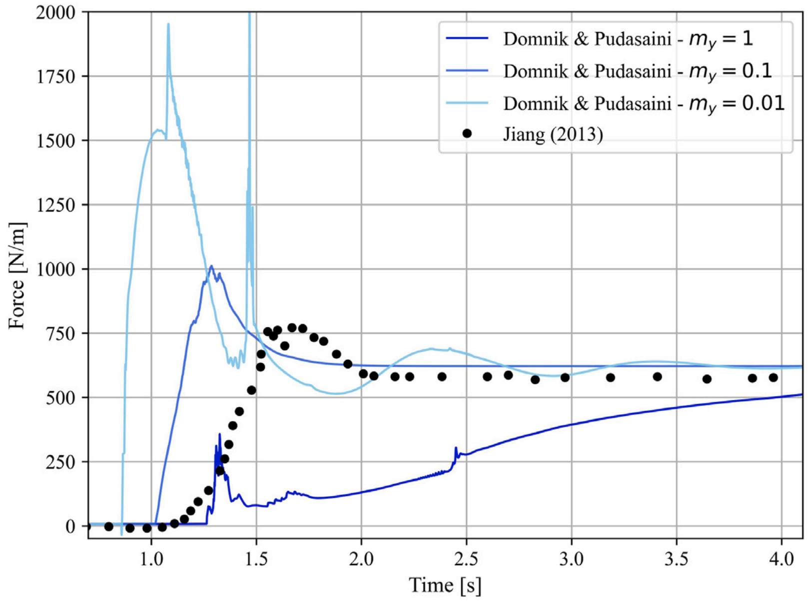

Fig. 4. Variation of the force evolution for an impact of dry granular material with a wall in an inclined flume (H = 0.15 m). Experimental data from Jiang and Towhata (2013) is displayed in black dots. m_y = [0.01 (light blue), 0.1 (blue), 1 (dark blue)] s.

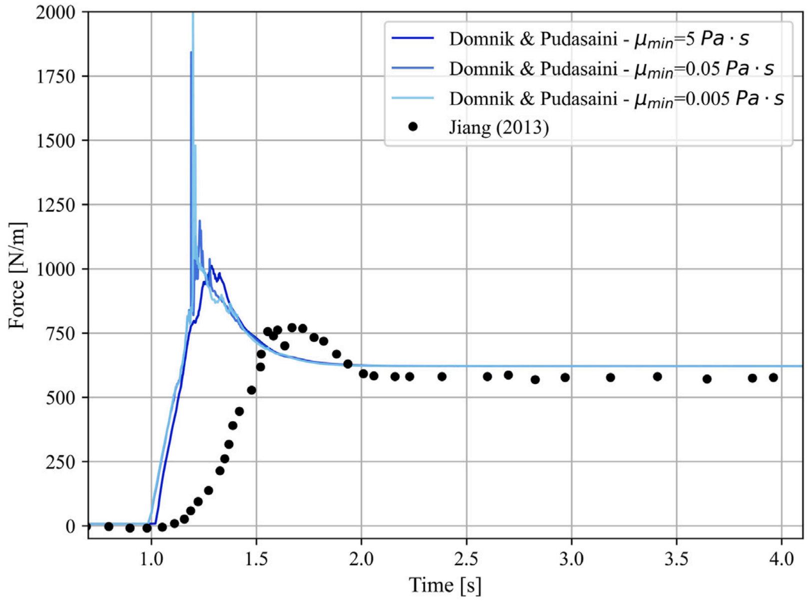

Fig. 5. Variation of the force evolution for an impact of dry granular material with a wall in an inclined flume (H = 0.15 m). Experimental data from Jiang and Towhata (2013) is displayed in black dots. μ_{min} = [0.005 (light blue), 0.05 (blue), 5 (dark blue)] Pa ·s.

decision to employ LES is supported by Li and Fuhrman (2022), who showed that the breaking point and the peak force on a vertical cylinder under incipient breaking are not expected to depend on the turbulence-closure choice, provided the model is stable and the simulations are well converged. In the present case, LES is particularly appropriate because the impact of granular material on a slender cylinder is expected to generate pronounced vortical structures; LES resolves these larger structures while filtering the smaller scales, thereby reducing the computational burden relative to DNS.

4.1. Force on a slender cylinder

To test the capability of the numerical approach to reproduce forces induced by granular landslides on a cylinder, a similar NWT as described in Romano et al. (2023) has been used, with the difference that a fully 3D case is considered. The geometry of the NWT is based on the experimental wave basin described by Grilli et al. (2017), with a slight modification made to increase the width of the NWT in order to avoid reflections from the side walls when a cylinder is added. The NWT is depicted in Fig. 10 and is 2.0 m long, 0.8 m wide, and 0.5 m

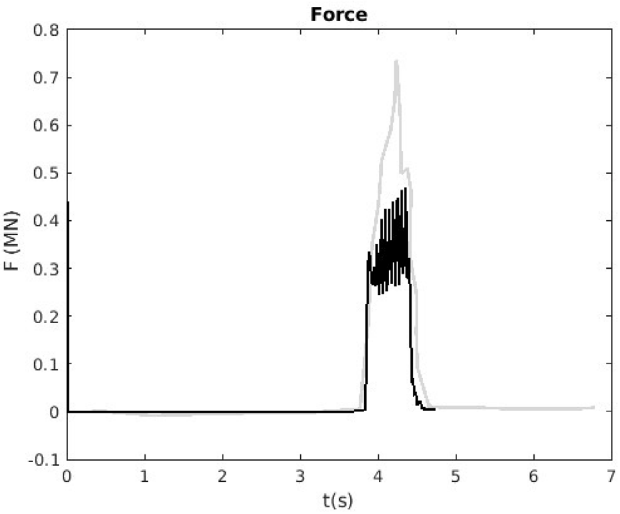

Fig. 6. Force evolution for debris avalanche that impacts a bridge pie. Gray light continuous line, numerical data from Zhong et al. (2022) and black continuous line, present work.

high. A slope (slope angle $\theta = 35°$) is placed at one edge of the flume. Granular landslides are modeled by a volume of glass beads (density $\rho = 2500$ kg/m3). In each experiment, a mass of beads was submerged in fresh water (density $\rho = 1000$ kg/m3), in a triangular reservoir located on the slope, fronted by a gated sluice. The initial water level (IWL) is set at 0.33 m.

The same numerical parameters as described by Romano et al. (2023) will be used, placing a cylinder of radius $r = 0.05$ m and height $h = 0.4$ m, in the middle of the NWT (plane XZ, Y = 0 m), $d_0 = 0.025$ m far from the ramp toe. The center point of the circular base of the cylinder is located at $XYZ = [0.82, 0.4, 0.0]$m.

The left patch is defined as a no-slip boundary, and absorption (shallow water active absorption boundary) has been set at the right patch of the domain. Walls are defined as slip boundaries, the bottom, ramp and cylinder as a nonslip boundary, and the top as an open boundary.

A preliminary grid refinement study C is carried out to select a mesh that efficiently combines accuracy and computational cost. The domain is characterized by a cell resolution of 0.006 m along the x direction, 0.006 m along the y direction, and 0.008 m along the z direction.

4.1.1. Turbulence modeling analysis

After a preliminary grid analysis, a comparative between the forces exerted by the cylinder depending on different turbulent modeling (LES, DES and $RANS$) is carried out, as distinct differences between the turbulence models surpass the influence of the grid.

The standard OpenFOAM LES wall functions (ESI-Group (2023)) are used to model the near-wall regions in the present work. The interactions of generated waves with the granular material are not quantified, and this is a limitation of the present work.

The same grid size will be used for the three cases (cell discretization of mesh $M2b$, from Table C.6 in Appendix C). All the numerical parameters from the previous NWT will be used, except of those which depend on the turbulence modeling.

For $RANS$ turbulence modeling, the $\kappa\omega - SST$ turbulence model has been selected, with an enhancement of Larsen and Fuhrman (2018) to limit the overproduction of turbulence under surface waves ($\lambda = 0.05$). The values of the model coefficients are: $\alpha_{k1} = 0.85$; $\alpha_{k2} = 1.0$; $\alpha_{w1} = 0.5$; $\alpha_{w2} = 0.856$; $\beta_1 = 0.075$; $\beta_2 = 0.0828$; $\beta_* = 0.09$; $\gamma_1 = 5/9$; $\gamma_2 = 0.44$; $a_1 = 0.31$; $b_1 = 1.0$; $c_1 = 10.0$. Standard OpenFOAM $RANS$ wall functions (ESI-Group (2023)) are used to model the region near the wall.

For the DES turbulence modeling, the SpalartAllmarasDDES turbulence model has been selected, Spalart et al. (2012), and the values of the model coefficients are: $k = 0.41$; $\sigma_{\mu t} = 2/3$; $C_{b1} = 0.1355$; $C_{b2} = 0.622$; $C_{w1} = C_{b1}/k^2 + (1 + C_{b2} / \sigma_{\mu t})$; $C_{w2} = 0.3$; $C_{w3} = 2$; $C_{v1} = 7.1$; $C_s = 0.3$; $C_{DES} = 0.65$; $C_k = 0.07$; $C_{t3} = 1.2$; $C_{t4} = 0.5$; $f_w^* = 0.424$. Standard OpenFOAM DES wall functions (ESI-Group, 2023) are used to model the region near the wall.

For the LES turbulence modeling, the Smagorinsky turbulence model has been selected. The default coefficients are: $C.k = 0.094$ and $C_e = 1.048$. The Van Driest damping function is selected, with $\kappa = 0.41$, $Aplus = 26$ and $C_{delta} = 0.158$. Standard OpenFOAM DES wall functions (ESI-Group (2023)) are used to model the region near the wall.

The force evolution caused by the interaction of the granular landslide with the cylinder is plotted in Fig. 11, the $RANS$ results are plotted in black continuous line, DES in red continuous line, and LES in blue continuous line. It can be seen that the three approaches reproduce the maximum force at the same instant ($t = 0.41$ s) but with different maximum force values ($F_{max} = 28.87$ N for $RANS$, $F_{max} = 24.28$ N for DES and $F_{max} = 23.90$ N for LES). The $RANS$ approach overestimates the maximum force when compared with the other two more accurate approaches. $RANS$ differs 20.8% from the LES results and DES differs 1.6% from the LES results, which by definition is the more accurate approach, since it solves large flow structures.

The maximum y + values around the ramp and the cylinder are less than 25 for the DES simulation and less than 20 for the $RANS$ simulation. The final numerical mesh (2.3M cells) was partitioned to be run in parallel in 8 processors, taking 2.5 days for the LES case, 2.5 days for the DES case and 1 day for the $RANS$ case, to numerically simulate 1.5 s.

Therefore, because of the ability of the LES turbulence modeling to solve large flow structures has been selected to analyze the influence of the radius of the cylinder and a shift in its initial position in the maximum forces exerted by the interaction with granular landslides. These results are aligned with the findings of Li and Fuhrman (2022), as the position of the peak force is not influenced by the choice of turbulence model.

4.2. Forces on a slender cylinder varying the shape

A catalog of numerical simulations will be used to analyze the influence of the radios of the cylinder r_c on the exerted forces. Seven cylinders that vary the radios will be analyzed: $r_c = [0.01375, 0.0275, 0.036, 0.055, 0.073, 0.0825, 0.11]$ m. The height of the seven cylinders is kept constant ($h_c = 0.4$ m.) and the center of the base of the seven cylinders is placed in the same position, $XYZ = [0.82, 0.4, 0.0]$m.

Again, the NWT is 2.0 m long, 0.8 m wide, and 0.5 m high. A slope (slope angle $\theta = 35°$) is placed at one edge of the flume. Granular landslides are modeled by a volume of glass beads (density $\rho = 2500$ kg/m3). The initial water level (IWL) is set at 0.33 m. For all numerical experiments, the same mass of beads was submerged in fresh water (density $\rho = 1000$ kg/m3), in a triangular-shaped reservoir located on the slope, fronted by a sluice gate.

The same grid size will be used for the three cases (defined in Section 4.1.1). When the number of cells remains constant around the surface of the cylinder, the size of the cells decrease with a smaller radius of the cylinder (r_c). All the numerical parameters of Section 4.1 are used. Standard OpenFOAM wall functions are used to model the near-wall region.

The evolution of the force caused by the granular landslide in different cylinders, varying the radius, is plotted in Fig. 12. It can be seen that all the cases present a similar behavior: first with a decrease of the initial force, followed by a sudden increase in the forces caused by the impact, and then a constant reduction when the material is accommodated around the fixed structured.

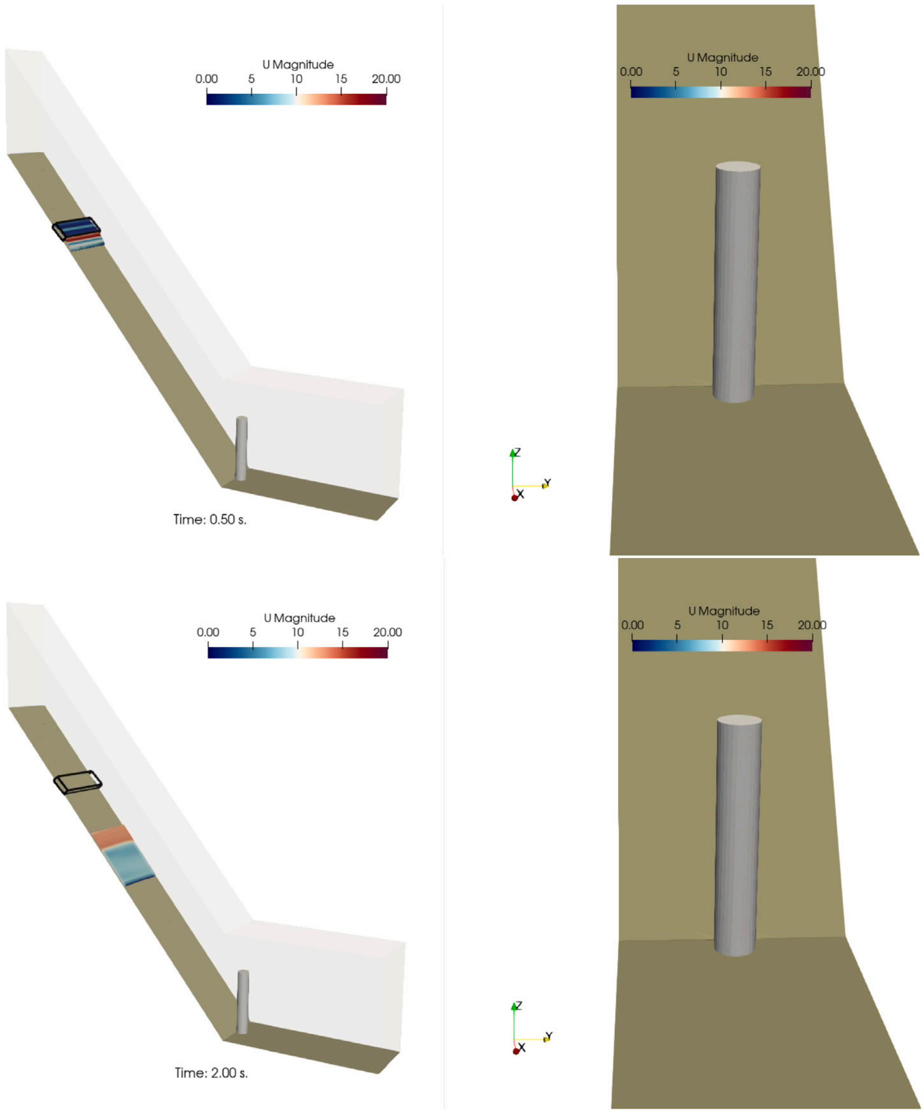

Fig. 7. Left panel, evolution of the granular landslide, plotting the velocity value on the interface material–air (VoF-granular = 0.5), right panel, 3D zoomed view, as described in Zhong et al. (2022). Times t = [0.50, 2.00, 4.00, 4.35] s., respectively. Initial position of dry granular material is presented with a black box.

As expected, larger r_c values produce larger forces, because the frontal area of the cylinder in which the granular landslide will impact is larger.

The maximum force is F_{max} = [8.32, 13.69, 16.25, 23.90, 26.55, 26.66, 28.99] N and occurs at t_{Fmax} = [0.43, 0.43, 0.43, 0.41, 0.41, 0.41, 0.41, 0.41] s for the seven tests. Therefore, as the radius is reduced, the maximum force is delayed in time because the frontal area of the cylinder is smaller, resulting in less refracted granular material.

Fig. 13 shows that the proposed fitting laws are able to describe the arrangement of the fitted data with good accuracy. It can be seen that there is a quadratic relationship between the maximum force (F_{max}) exerted by the granular landslide on the cylinder and the radius of the cylinder (r_c). This is also confirmed by the determination coefficient, $R^2 = 0.89$.

The maximum y + values around the ramp and the cylinder are less than 30 for the seven simulations. The Pope (2000) criterion of the quality of the LES simulation (M) for water is above 0.8 in the vicinity of the cylinder, in the ramp and in the interface granular material–water. All the numerical meshes (2.3M cells) were partitioned to be run in parallel in 8 processors, taking 2.5 days to numerically simulate 2 s.

4.2.1. Landslide evolution

Fig. 14 is used to illustrate the relation due to the maximum forces exerted on the cylinder ($r_c = 0.55$ m) and the evolution of the granular landslide. Because the variation of the radius does not significantly affect the displacement of the material, only the most representative case is analyzed.

Six gauges are placed in the NWT to track the displacement of the landslide, x = [0.66, 0.725, 0.745, 0.765, 0.8775, 0.90] m. The first three sensors are placed to track the evolution of the material when sliding through the ramp (the third one is placed on the toe of

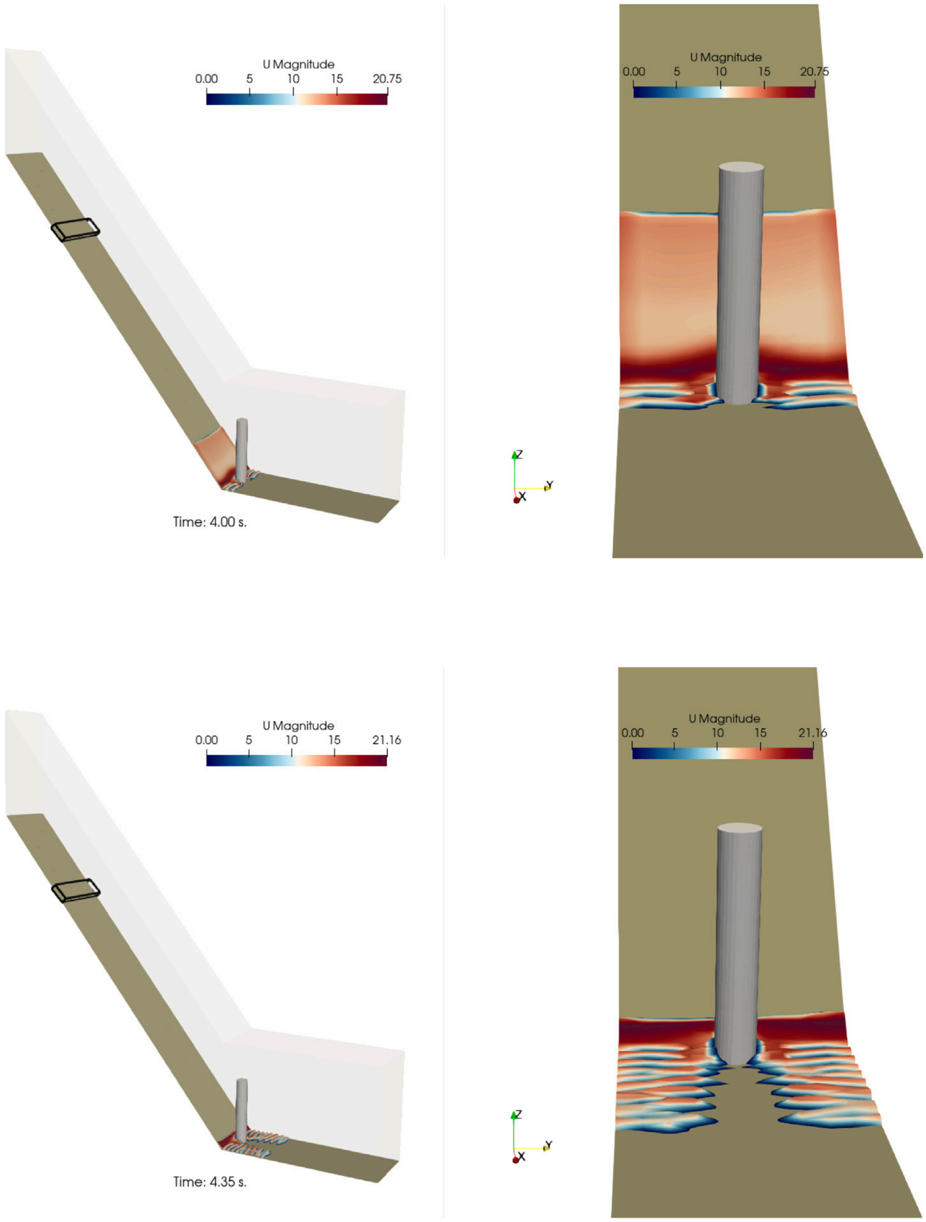

Fig. 7. (*continued*).

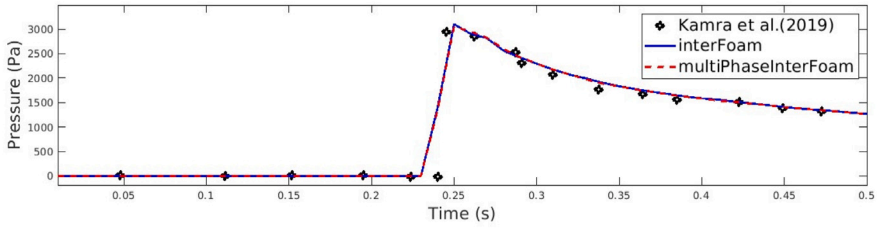

Fig. 8. Plot of the pressure measurement on the cylindrical obstacle. Numerical data in black circles Kamra et al. (2019), numerical data from *interFoam* (blue continuous line) and numerical data from *multiPhaseInterFoam* (red dashed line).

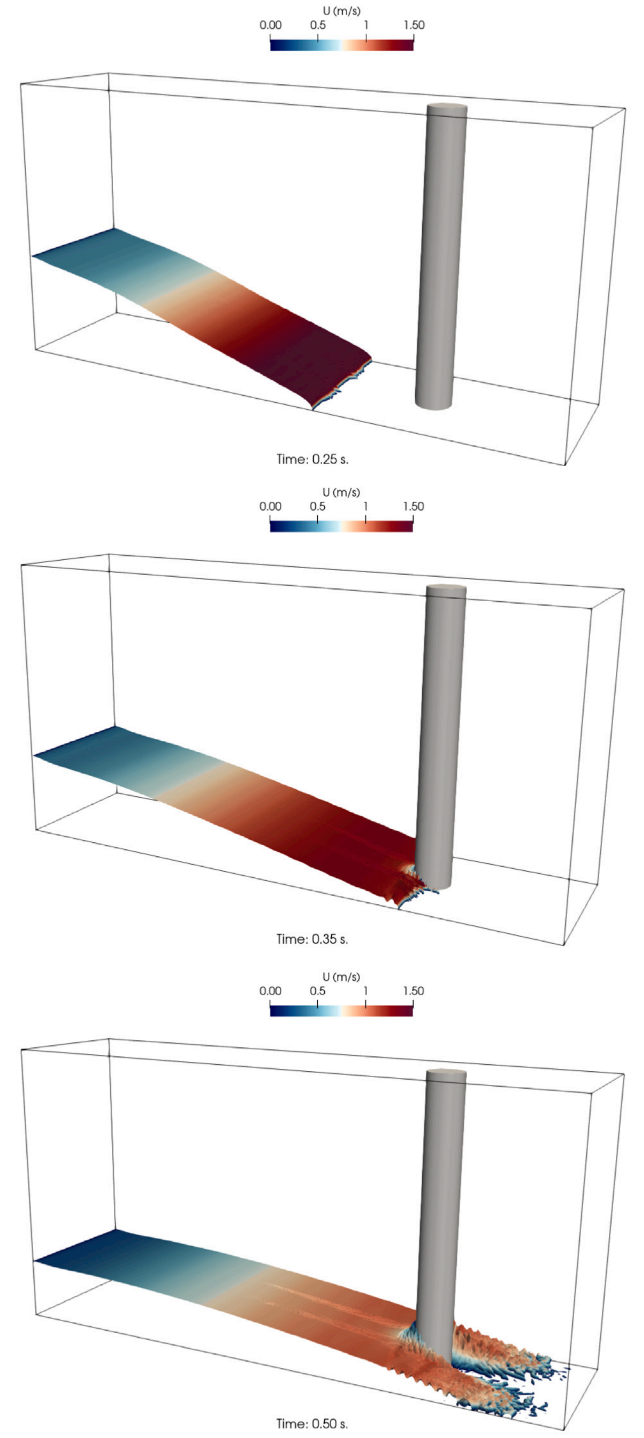

Fig. 9. 3D view of the impact of the granular material in a cylinder. Velocity magnitude plotted over the interface material–air (VOF-debris=0.5). Times t = [0.25, 0.35, 0.5]s., respectively.

the ramp). The fourth sensor is placed in the vicinity of the cylinder to capture the instant of impact. The last two sensors are placed to estimate the time it takes for the granular material to deposit after the cylinder.

From x = 0.66 m, x = 0.375 m, and x = 0.750 m (first, second, and third plots), the evolution of the landslide is depicted when sliding through the ramp. As the material slides and displaced the still water, a force is exerted on the cylinder before the material has impacted on the cylinder. The maximum accumulations are η_l = 0.17 m for gauge placed at x = 0.66 m (t = 0.16 s), η_l = 0.13 m for gauge placed at x = 0.725 m (t = 0.34 s) and η_l = 0.12 m for gauge placed at x = 0.745 m (t = 0.45 s). From x = 0.760 m (fourth plot), it is visualized that the maximum force (F_{max}) is exerted when the landslide hits the cylinder (t_{max} = 0.41 s). The granular material will accumulate in the windward part of the cylinder but does not increase the maximum force. The maximum accumulation is η_l = 0.10 m for the gauge placed at x = 0.0.765 m (t = 0.83 s). From x = 0.8775 m and x = 0.90 m (fifth and sixth plots), it is visualized when the granular material reaches the leeward side of the cylinder and starts to deposit. Again, it does not contribute to increasing the forces on the cylinder that are mainly exerted by the material on the windward side of the cylinder. From the six plots, it can be seen that the granular material remains without any variation after 1.6 s, so it has reached a steady state. The maximum accumulations are η_l = 0.018 m for gauge placed at x = 0.8775 m (t = 1.53 s) and η_l = 0.043 m for gauge placed at x = 0.90 m (t = 1.9 s).

4.2.2. Fluid flow structures

When submerged landslides interact with an obstacle, complex fluid flow structures are created that can be analyzed and studied with CFD techniques. Large-scale turbulence structures are commonly defined as regions in space (or time) within which the flow field has a characteristic coherent flow pattern (Pope (2000)). Depending on the different physical mechanisms, coherent structures have different shapes. In fact, because of the presence of a cylinder, the shape of which is circular, the fluid flow forms a Horseshoe Vortex (HV) system upstream and a boundary layer detachment, as well as complicated vortex shedding at the wake of the structure.

As stated in Gilletta et al. (2025), the adverse pressure gradient generated by an obstruction of the flow caused by an obstacle forms a downward flow, then a reverse flow that competes with the upstream steady current, leading to a system of multiple HVs that swirl around the span direction.

Fig. 15 is used to illustrate the flow structures during the landslide for r_c = 0.55 m, presenting in the left panel, a 3D view of the granular landslide velocities and Q-criterion (green), and in the right panel, a 2D view of the granular landslide velocities and Q-criterion (green) in the vicinity of the cylinder, for seven time steps t = (0.60 s, 0.90 s, 1.05 s, 1.50 s, 1.90 s. 2.30 s and 2.80 s).

The first image, t = 0.60 s, presents an HV induced by an adverse gradient, generated by an obstruction of the flow when the granular material interacts with the slender cylinder. The development of HV reveals lifts, stretches, ejections, and sweeps, which play a central role in hydrodynamics around the structure (Salim et al. (2017)). The images t = 0.90 s and t = 1.05 s reproduce the evolution of the HV and how it changes shape and how it slowly is being displaced. Next, in t = 1.50 s it can be seen that the HV is ejected and lifted off the ground and the granular material. And finally, simultaneously breakup and burst occurs near the free surface (t = 1.98 s, t = 2.30 s and t = 2.80 s).

A remarkable result analyzing qualitatively the coherent structures is that they are symmetric with respect to y = 0.0 m, indicating that the numerical approach is accurate and robust, as it can reproduce these complex flows very precisely. From Fig. 15 it can be seen that grooves appear in the free surface of the granular material. This is a limitation of the present numerical setup, which is related to $MULES$, the algorithm that tracks the position of the free-surfaces for the fluids (Qwist and Christensen (2023)).

4.3. Forces on a slender cylinder varying the position

A catalog of numerical simulations will be used to analyze the influence of the displacement of the cylinder (d) from the toe of the ramp. Six cases varying the distance will be analyzed: d = [0.0, 0.025, 0.05, 0.075, 0.15, 0.25] m. The height of the six cylinders is kept

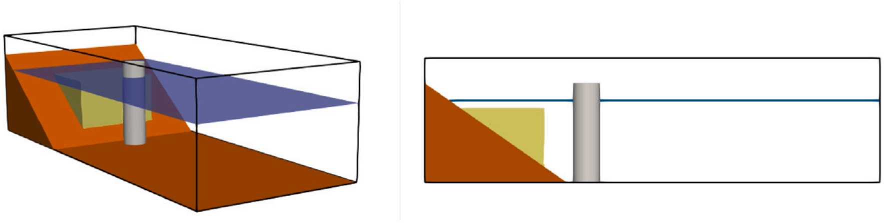

Fig. 10. Left panel, 3D view of the NWT; Right panel, 2D view of the NWT, plane XZ (y = 0 m). Cylinder of radius $r = 0.055$ m. and height $h = 0.4$ m., placed $d_0 = 0.025$ m. far from the toe of the ramp. In yellow, the granular material, in blue the initial water level (IWL = 0.33 m.).

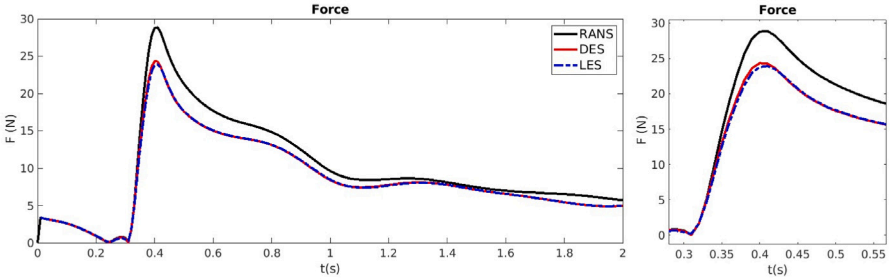

Fig. 11. Left panel: Force evolution over the time selecting different turbulence models, $RANS$(black continuous line), DES(red continuous line) and LES(blue dashed line). Right panel: zoomed view of the instant of impact.

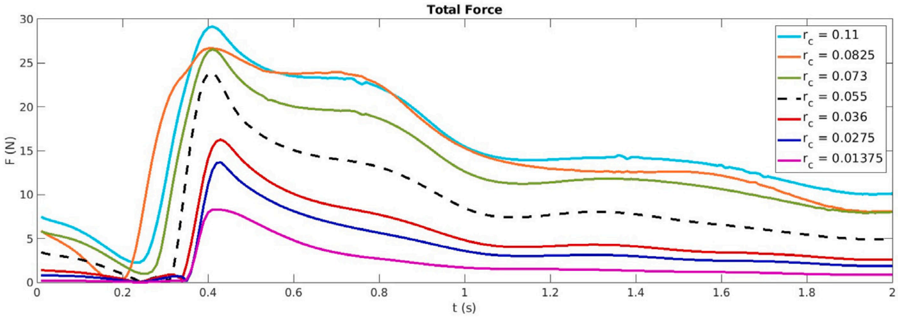

Fig. 12. Force evolution over the time for different values of the radius of the cylinder, r_c = [0.01375, 0.0275, 0.036, 0.055, 0.073, 0.0825 and 0.11] m.

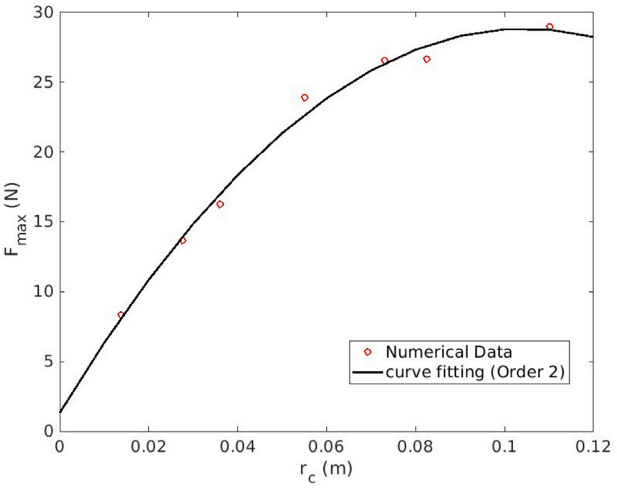

Fig. 13. Plot of the maximum force (F_{max}) exerted by the granular landslide in the cylinder, as a function of the radius (r_c) of the cylinder. Numerical data in red circles, curve fitting or order 2 in black continuous line.

constant (h_c = 0.4 m). The center of the base of the five cylinders is placed in the middle of the spam-wise direction (Y = 0.0 m), being displaced d in the stream-wise direction.

Again, the NWT is 2.0 m long, 0.8 m wide, and 0.5 m high. A slope (slope angle $\theta = 35°$) is placed at one edge of the flume. Granular landslides are modeled by a volume of glass beads (density $\rho = 2500$ kg/m3). The initial water level (IWL) is set at 0.33 m. For all numerical experiments, the same mass of beads was submerged in fresh water (density $\rho = 1000$ kg/m3), in a triangular-shaped reservoir located on the slope, fronted by a sluice gate.

The same grid size ($M3c$) will be used for the three cases (defined in Section 4.1.1), with an equal number of cells around the surface of the cylinder. All the numerical parameters of Section 4.1 are used.

The evolution of the force caused by the granular landslide, which varies the distance from the cylinder to the toe of the ramp, is shown in Fig. 16. It can be seen that there are different behaviors depending on the distance from the toe of the ramp to the cylinder.

When the landslide starts to slide down the slope, the velocity of the landslide increases. If the distance to the cylinder (impact point) is short, the landslide front is compact, so most of the granular material will interact with the structure creating maximum strain. In contrast, if the distance to the cylinder is increased, the landslide front is thinner at the impact point because there is enough space for the granular material to be deposited in the span-wise direction, so the force exerted on the cylinder will decrease significantly. The maximum forces are

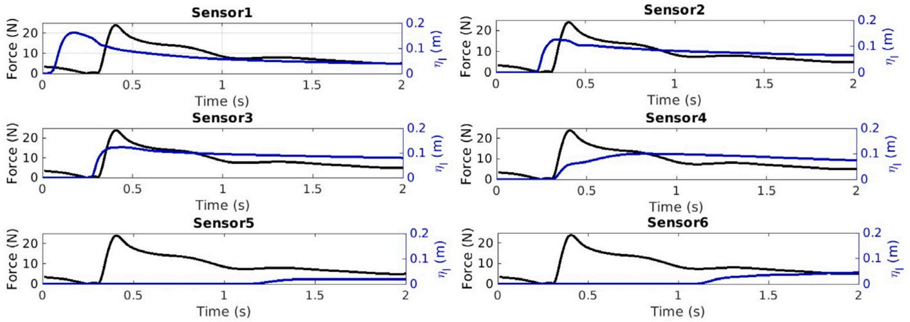

Fig. 14. Plot of the maximum force (F_{max}) exerted on the cylinder (black continuous line), and the evolution of the granular landslide (blue continuous line) in six positions (x = [0.66, 0.725, 0.745, 0.765, 0.8775, 0.90]m).

F_{max} = [23.90, 20.38, 16.50, 11.92, 5.19, 3.26] N for d = [0, 0.025, 0.050, 0.075, 0.15, and 0.25] m at t_{max} = [0.41, 0.43, 0.47, 0.49, 1.59, 1.78] s.

For d = 0.0 m it can be observed that a maximum force is created after a constant increase of the force on the cylinder. When the cylinder is slightly displaced, d = [0.025, 0.050, and 0.075] m, the exerted force is similar to the first case (d = 0.0 m), but delayed in time and reduced in magnitude. In all these three cases, there is a maximum force (F_{max}) that is achieved after a constant increase in the force resulting from the sudden impact of the granular material on the cylinder. For d = 0.025 m, F_{max} = 20.38 N at t_{max} = 0.43 s. For d = 0.05 m, F_{max} = 16.50 N at t_{max} = 0.47 s. For d = 0.075 m, F_{max} = 11.92 at t_{max} = 0.49 s. For these first four displacement values, d = [0.0, 0.025, 0.05, 0.075] m, there is a linear relationship (Fig. 17) between the maximum force (F_{max}) exerted by the granular landslide in the cylinder and when it occurs (t_{max}). This is also confirmed by the determination coefficient, R^2 = 0.97.

For d = 0.15 m and d = 0.25 m, there is no clear trend of the evolution of the force. For d = 0.15 m there is a constant increase of the force and then a sudden decrease of the forces to a minimum value (t = 0.6 s and F = 0.44 N, followed by a new increase until it reaches its maximum (t_{max} = 1.59 s and F_{max} = 5.19 N). First, the granular material displaces calm water and induces a wave that will propagate toward the open sea, producing the aforementioned constant increase in the force. Once the wave has propagated, and after reflection and refraction with the structure, there is a decrease in the water level, which will induce a reduction of the force to a minimum value. Finally, the granular material will impact the cylinder, it will accumulate and deposit in the vicinity of the structure, resulting in an increase in the force. For d = 0.25 m, the evolution of the force over time depicts a series of oscillations, produced by displaced water and the impacts and arrangement of the granular material in a wide region before the cylinder. The maximum force F_{max} = 3.26 N occurs at t_{max} = 1.78 s.

Fig. 18 shows that the proposed fitting laws are able to describe the arrangement of the fitted data with good accuracy. It can be seen that there is a quadratic relationship between the maximum force (F_{max}) exerted by the granular landslide on the cylinder and the distance (d) from the toe of the ramp to the cylinder. This is also confirmed by the coefficient of determination, R^2 = 0.99.

The maximum y + values around the ramp and the cylinder are less than 30 for the six simulations. The Pope (2000) criterion of the quality of the LES simulation (M) for water is above 0.8 in the vicinity of the cylinder, in the ramp and in the interface granular material-water. All the numerical meshes (2.3M cells) were partitioned to be run in parallel in 8 processors, taking 2.5 days to simulate 2 s.

4.3.1. Landslide evolution

Fig. 19 is used to illustrate the relation due to the maximum forces exerted on the cylinder (r_c = 0.55 m) and the evolution of the granular landslide, for the six cases varying the distance of the cylinder to the toe of the ramp d = [0.0, 0.025, 0.05, 0.075, 0.15 and 0.25]m, in the sensor placed in x = (0.765+d) m. It shows that the maximum force is diminished when the cylinder is distanced from the toe of the ramp because of the amount of granular material accumulated in the vicinity of the cylinder. It can be detected that when the cylinder is near the toe of the ramp (first panel, d = 0 m), there is an impact of the granular material on the cylinder that creates a steep increase in material on the windward side, followed by deposition and accumulation. At t = 0.32 s, there is no material in the vicinity of the cylinder, and at t = 0.41 s the maximum force is exerted, with η_l = 0.58 m, measured from the ground to the interface material-water. The maximum accumulation η_l = 0.1 m occurs at t = 0.83 s.

As the cylinder is being displaced from the toe of the ramp (second, third, and fourth panels, representing d = [0.025 m 0.05, 0.075] m), the steepness of the increase is reduced and the evolution becomes more gentle, because some of the material is deposited in the span-wise direction and does not interact with the cylinder. For d = 0.025 m, at t = 0.36 s, there is no material in the vicinity of the cylinder, and at t = 0.67 s the maximum accumulation is achieved, η_l = 0.08 m. For d = 0.05 m, at t = 0.41 s, there is no material in the vicinity of the cylinder and at t = 0.92 s the maximum accumulation is achieved, η_l = 0.07 m. For d = 0.075 m, at t = 0.44 s, there is no material in the vicinity of the cylinder, and at t = 1.5 s the maximum accumulation is achieved, η_l = 0.065 m.

Finally, when the cylinder is far from the toe of the ramp (d = [0.15, 0.25] m), the material deposits and accumulates gently on the windward side of the cylinder, resulting in a constant increase in force. Maximums accumulations are η_l = 0.042 m for case d = 0.15 m (t = 2 s) and η_l = 0.026 m for case d = 0.25 m (t = 2 s).

5. Conclusions

This study has presented a detailed numerical investigation of the impact of submerged granular landslides on structures within the OpenFOAM framework. By combining a viscoplastic Coulomb rheology with multiphase solvers, the model was able to reproduce benchmark laboratory experiments and capture the essential dynamics of granular impact processes. The numerical results successfully described both the peak forces generated during sudden impacts and the subsequent flow evolution, including the deposition and the development of stagnant zones. The outcomes confirm that the simplified single-phase approach, when properly calibrated, can provide physically meaningful predictions of

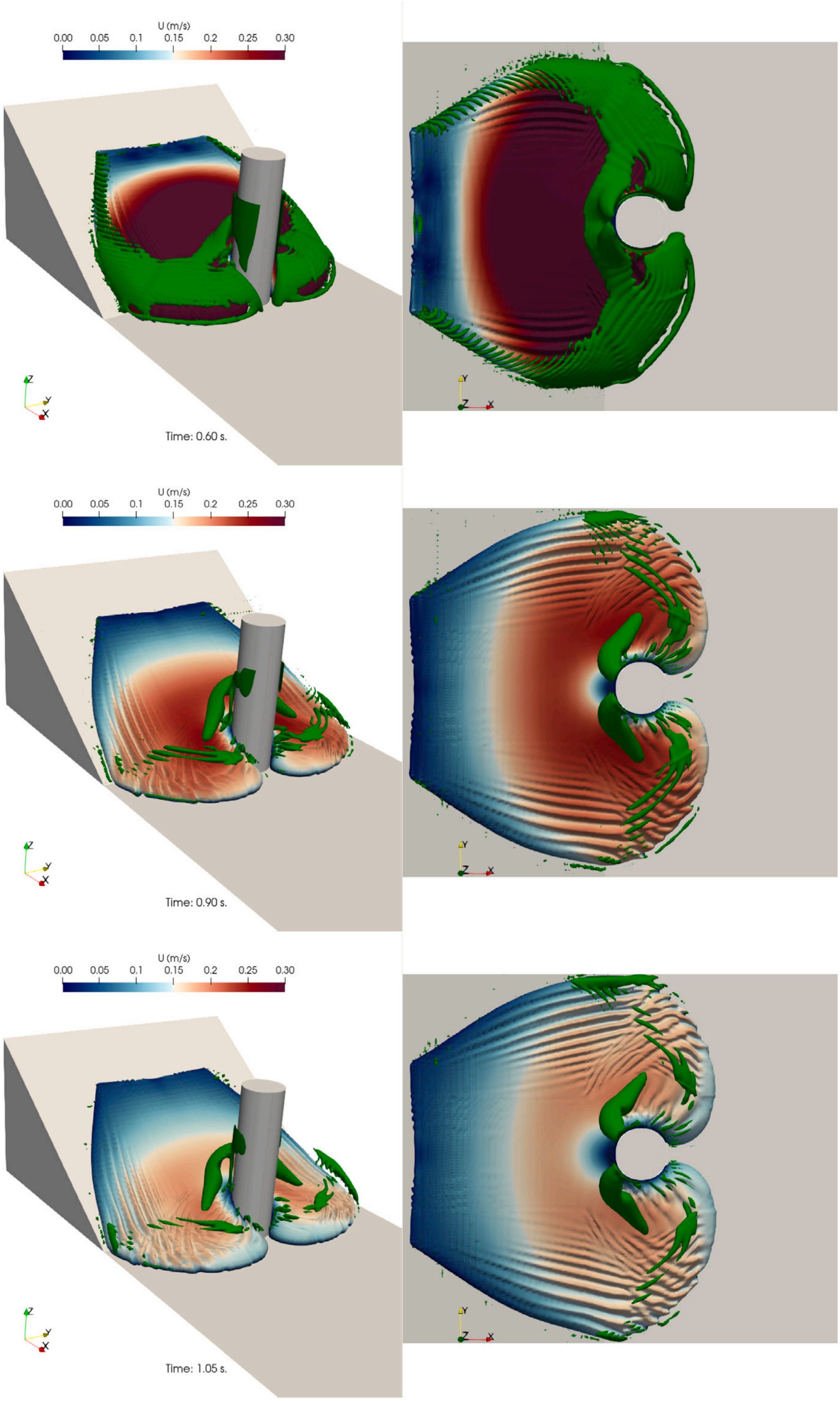

Fig. 15. Left panel, 3D view of the granular landslide velocities and Q-criterion (green). Right panel, 2D view of the granular landslide velocities and Q-criterion (green) in the vicinity of the cylinder. Times t = (0.60, 0.90, 1.05, 1.50, 1.90, 2.30 and 2.80)s., respectively.

global forces and kinematics, at a computational cost significantly lower than more complex two-fluid or particle-resolved methods.

The validation strategy adopted here, which isolates individual physical processes and compares them with established experimental benchmarks, proved essential to reduce uncertainty. Instead of attempting to validate the full complexity of a submerged landslide in one step, the model was proved with simplified cases: dry granular impacts, three-dimensional slides against piers, and fluid dam-breaks. This

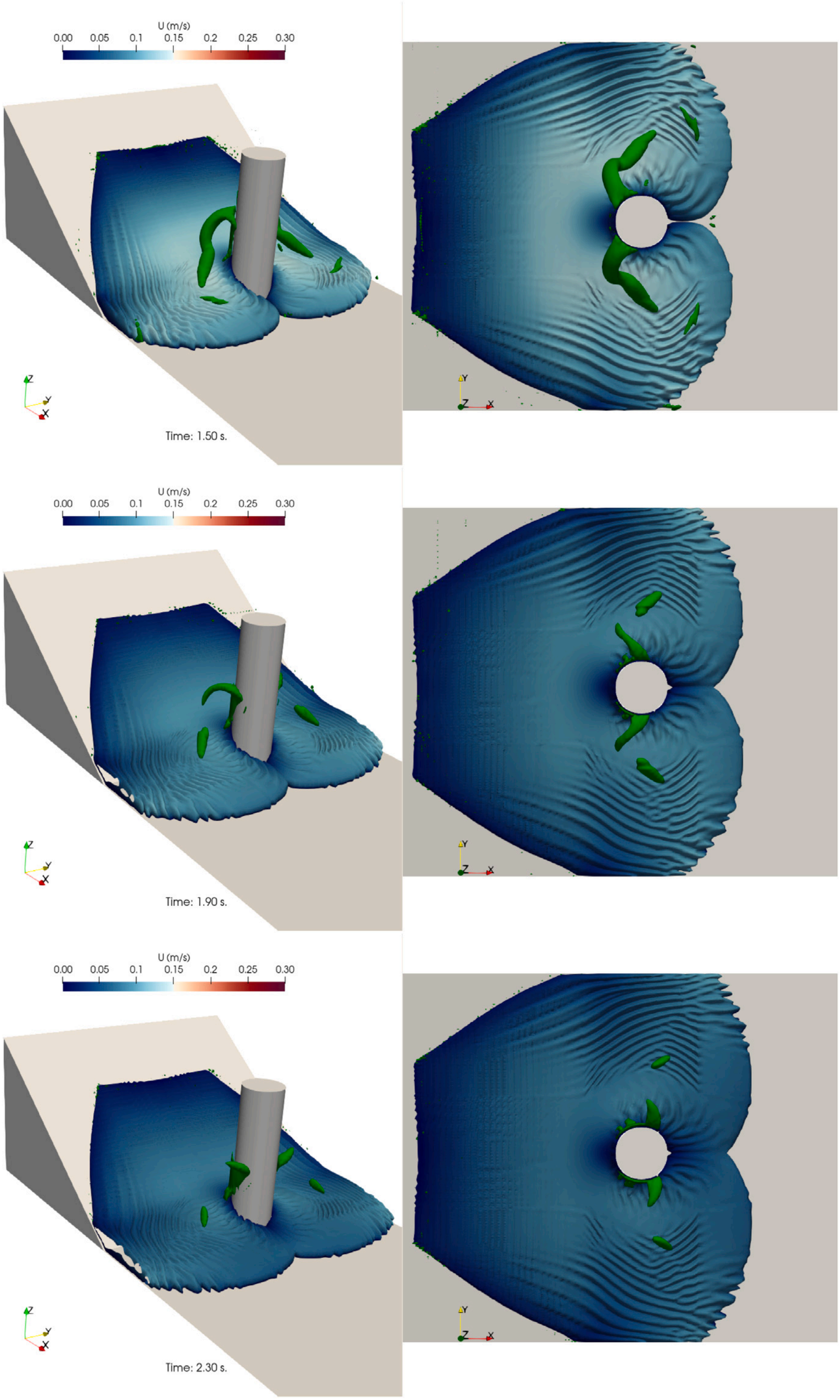

Fig. 15. (*continued*).

modular validation confirmed that the solver can reproduce the most relevant building blocks of the problem, such as impact force histories and deposition patterns. The approach also highlighted specific areas where the model tends to diverge from reality, for instance in the rate of force decay after impact, where micro-scale effects not represented in the continuum formulation play a role. Such systematic testing strengthens confidence in the model's predictive power while providing a road map for future improvements.

It is important to situate the present approach within the broader landscape of numerical methods for granular flows. Two-fluid Eulerian models, which resolve both phases with interpenetrating continua and explicit drag laws, can capture pore-pressure transients and phase

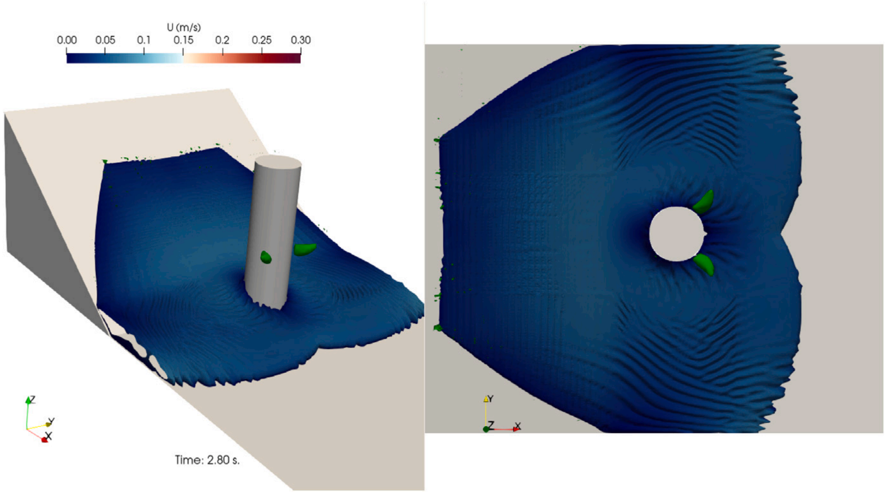

Fig. 15. (*continued*).

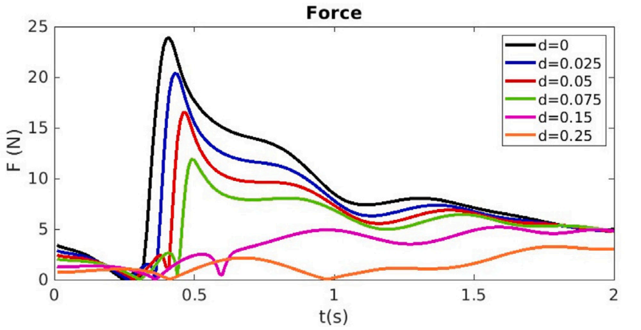

Fig. 16. Force evolution over the time for different distance of cylinder to the toe of the ramp, d = 0.0 m (black continuous line), d = 0.025 m (blue continuous line), d = 0.05 m (red continuous line), d = 0.075 m (green continuous line), d = 0.15 m (purple continuous line) and d = 0.25 m (orange continuous line).

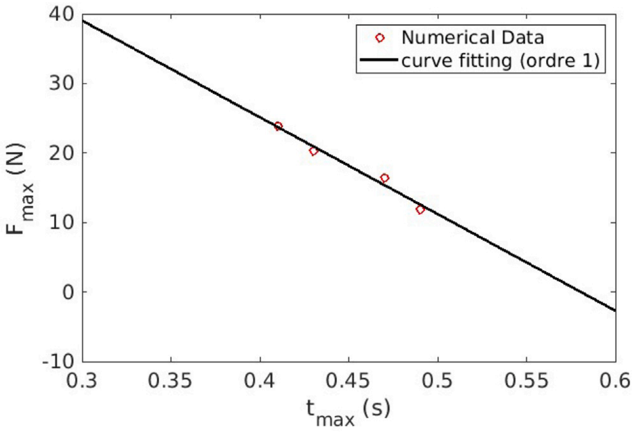

Fig. 17. Plot of the maximum force (F_{max}) exerted by the granular landslide in the cylinder, as a function of the time (t_{max}) for the first four cases (d = [0.0, 0.025, 0.05, 0.075] m). Numerical data in red circles, curve fitting of order 1 in black continuous line.

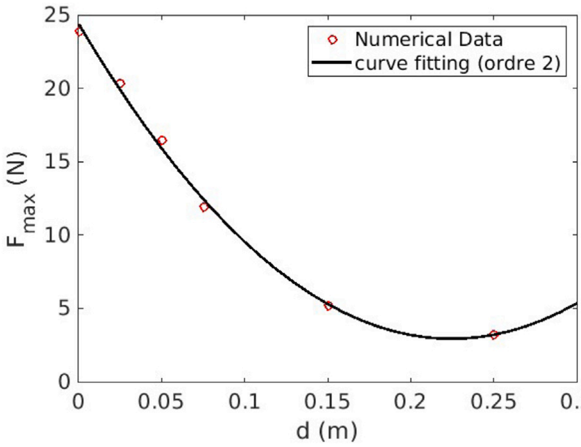

Fig. 18. Plot of the maximum force (F_{max}) exerted by the granular landslide in the cylinder, as a function of the distance (d) of the toe of the ramp to the cylinder. Numerical data in red circles, curve fitting of order 2 in black continuous line.

slip, offering more detailed insight into fluid–grain interactions. Grain-resolved CFD–DEM, at the other end of the spectrum, provides the highest physical fidelity by modeling individual particle contacts, dilatancy, and peak local loads. However, both approaches are orders of magnitude more computationally demanding, often making them impractical for full-scale engineering scenarios. The present LES–continuum framework occupies an intermediate position: it sacrifices grain-scale detail but gains tractability and robustness, enabling its application to realistic problems such as the design of offshore piles and platforms subject to submarine landslide hazards.

Despite these advances, the study has clear limitations. The single-phase continuum rheology does not resolve pore-pressure evolution, hydroplaning, or transient fluid–solid slip, which are known to play a role in submerged landslide dynamics. The choice of boundary conditions and mesh resolution inevitably constrains the ability to capture the smallest scales of turbulence, particularly near walls and in thin shear bands. Moreover, the validations performed, while systematic, are limited in number and scope; additional comparisons with large-scale flume or centrifuge experiments would further strengthen the

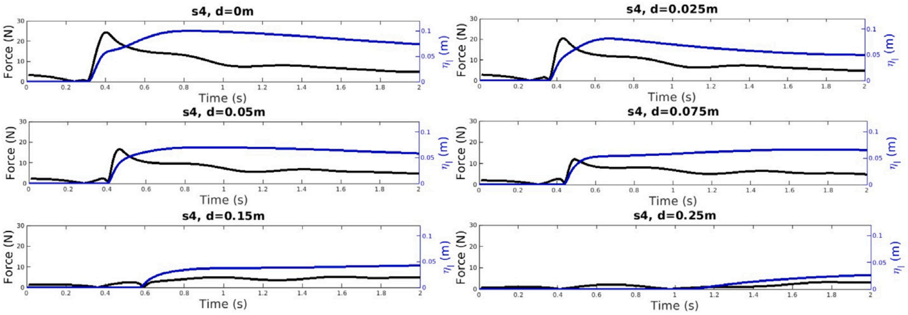

Fig. 19. Plot of the maximum force (F_{max}) exerted on the cylinder (black continuous line), and the evolution of the granular landslide (blue continuous line), for different distance of cylinder to the toe of the ramp, d = [0.0, 0.025, 0.05, 0.075, 0.15 and 0.25] m., in one single position x = (0.765+d) m.

credibility of the approach. These limitations should not be viewed as flaws, but as reminders of the trade-offs inherent in modeling complex geophysical flows.

An important modeling decision in this work is the choice of rheological closure for the granular phase. Although it is not the objective of the present study to provide an exhaustive comparison of granular rheologies, two commonly used closures were considered in the literature review and selectively tested here. These are the viscoplastic Coulomb rheology (more suitable for wet granular flows) and the μ(I) rheology (more suitable for dry dense granular flows). The comparison in the dry benchmark showed that these approaches differ in their predictive capacity depending on the phenomenon of interest. The μ(I) rheology, with its explicit dependence on the shear rate and pressure, enhances the description of transient forces and is particularly effective in capturing the intensity and timing of peak loads. In contrast, the viscoplastic Coulomb formulation is better suited to represent runout cessation, stagnant regions, and the morphology of final deposits. These complementary strengths underscore the broader lesson that no single rheology can universally capture the entire spectrum of granular flow behaviors. Rather, the choice of model should be dictated by the objectives of the simulation and by the level of physics represented in the framework. In the present single-phase VoF approach, μ(I) is therefore restricted to the dry benchmark comparison, while the viscoplastic Coulomb model is employed for both dry and submerged conditions.

From an engineering standpoint, the main contribution of this work lies in demonstrating that LES combined with simplified continuum rheologies can deliver accurate and computationally feasible predictions of impact loads on slender offshore structures. The approach is particularly well-suited for preliminary design studies, where multiple scenarios must be assessed quickly to evaluate risk envelopes. By capturing transient force peaks, the framework provides information essential for structural safety, while its ability to predict deposition patterns informs hazard mapping and site selection. The results therefore contribute to bridging the gap between advanced computational fluid dynamics and practical offshore engineering needs.

In conclusion, this study has shown that a carefully designed LES framework, equipped with a viscoplastic rheology and validated through modular benchmarks, can capture the essential dynamics of submerged granular landslide impacts. The analysis demonstrates not only the capabilities but also the limitations of the approach, emphasizing the importance of methodological choices in turbulence modeling, rheology selection, and validation strategy. The findings confirm that OpenFOAM provides a reliable and efficient tool for investigating extreme impact processes, while also pointing to future improvements that will further enhance its relevance for hazard assessment and infrastructure design.

Table A.1
Numerical grids used in the mesh sensibility analysis.

Mesh name	Discretization	Number of Cells
Mesh1 ($M1a$)	dx = 0.0103 m, dy = 0.3 m, dz = 0.0103 m	0.008M
Mesh2 ($M2a$)	dx = 0.0050 m, dy = 0.3 m, dz = 0.0050 m	0.041M
Mesh3 ($M3a$)	dx = 0.0035 m, dy = 0.3 m, dz = 0.0035 m	0.080M

CRediT authorship contribution statement

Gabriel Barajas: Writing – review & editing, Writing – original draft, Visualization, Validation, Software, Methodology, Investigation, Formal analysis, Data curation, Conceptualization. **Javier L. Lara:** Writing – review & editing, Resources, Project administration, Methodology, Investigation, Funding acquisition, Conceptualization. **Alessandro Romano:** Writing – review & editing, Supervision, Methodology, Investigation, Formal analysis, Data curation, Conceptualization. **Eduard Puig Montellà:** Writing – review & editing, Writing – original draft, Software, Methodology, Investigation, Formal analysis, Data curation.

Declaration of competing interest

The authors declare that they have no known competing financial interests or personal relationships that could have appeared to influence the work reported in this paper.

Appendix A. Grid analysis 1: dry granular flow impact on a inclined flume

A preliminary grid refinement study is carried out, following the approach described in Roache (1997), Stern et al. (2001) and Vukčević (2016). Three grids, $M1a$ (coarse mesh), $M2a$ (medium mesh) and $M3a$ (fine mesh) (Table A.1), are used to establish the total uncertainty arising from temporal and spatial discretization errors.

The maximum force exerted (F^m) on the wall is used as the significant quantity for each grid size. To analyze the convergence or divergence of the grid analysis, the discrimination ratio R_D is calculated as Vukčević (2016):

$$R_D = \frac{\left(F^m_f - F^m_m\right)}{\left(F^m_m - F^m_c\right)} \tag{A.1}$$

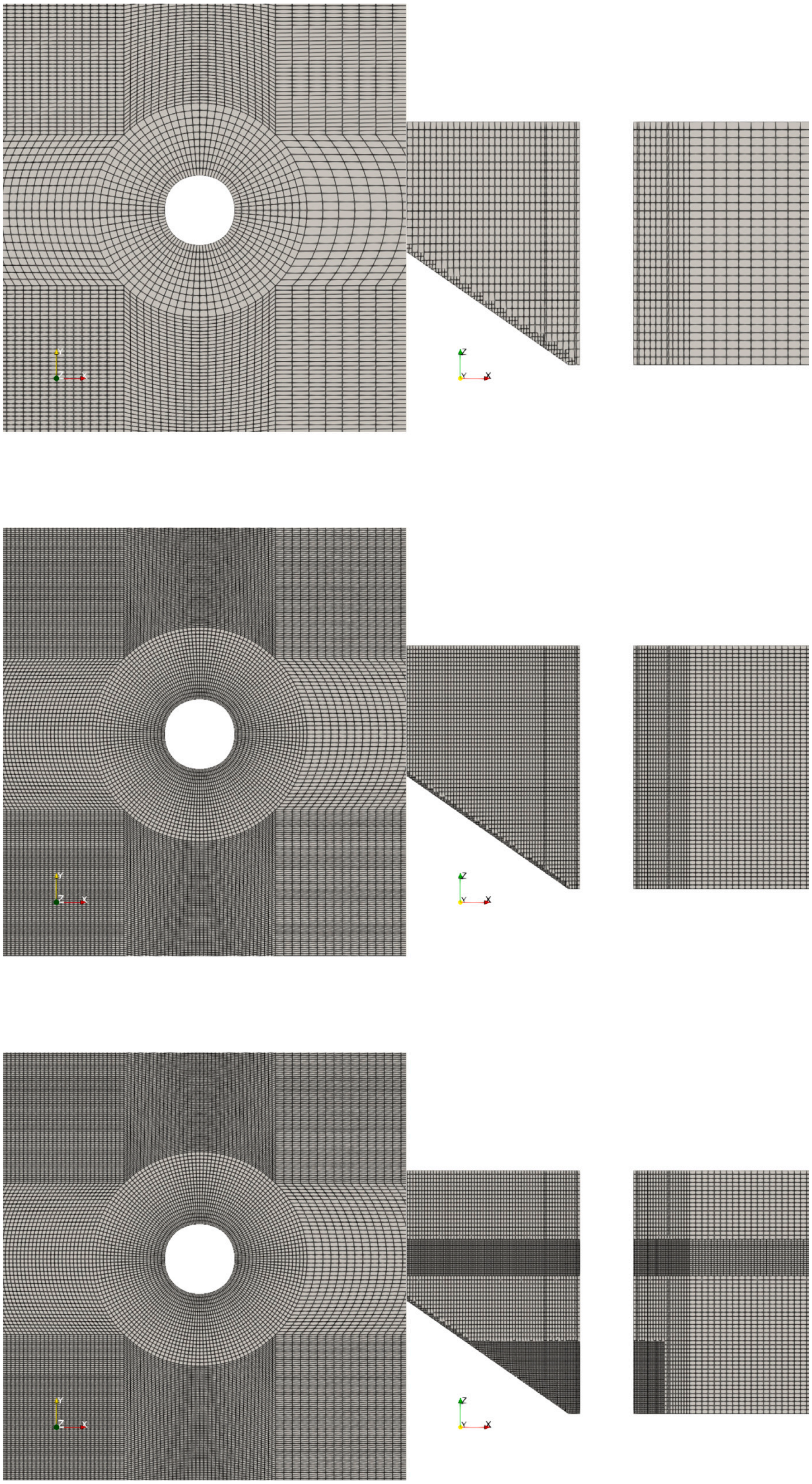

Fig. C.20. Cell size discretization (from C.6). Top panel, mesh $M1b$ (coarse), medium panel, mesh $M2b$ (medium) and bottom panel, mesh $M3b$ (fine). Left panels are a top views and right panels are side views (Plane XZ, y = 0.0 m).

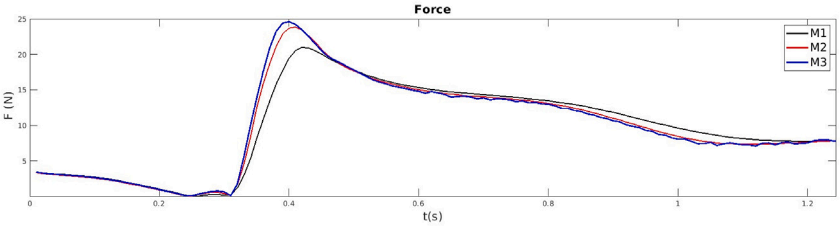

Fig. C.21. Force evolution over the time for three meshes used in the grid analysis, $M1$(black continuous line), $M2$(red continuous line) and $M3$(blue continuous line).

Table A.2
Convergence based on discrimination ratio R_D.

Type	Convergence	Divergence
Monotonic	$0 < R_D < 1$	$R_D < 0$ and $\|R_D\| < 1$
Oscillatory	$R_D > 1$	$R_D < 0$ and $\|R_D\| > 1$

Table A.3
Relative discretization uncertainty, U[%].

Parameter	$M1a$	$M2a$	$M3a$	U[%]
F^m	1456	1015	936	19.17

where F_f^m is the solution of the finest mesh ($M3a$), F_m^m is the solution of the medium mesh ($M2a$) and F_c^m is the solution of the coarser mesh ($M1a$). Table A.2 summarizes the four types of convergence.

The absolute grid uncertainty U_a, can be calculated for monotonic convergence:

$$U_a = F_s \frac{(F_f^m - F_m^m)}{(r^p - 1)}, \tag{A.2}$$

where F_s is the safety factor (1.5), r is the grid–refinement ratio between the medium and fine meshes, defined as $r = h_m/h_f$, with the representative grid size taken as $h = (\Delta x\,\Delta y\,\Delta z)^{1/3}$ for each mesh, and p is the order of accuracy, defined as:

$$p = min\left(\frac{\ln\left|\dfrac{F_f^m - F_m^m}{F_m^m - F_c^m}\right|}{\ln(r)}, 2 \right) \tag{A.3}$$

In the case of oscillatory convergence, the uncertainty is calculated as follows Stern et al. (2001):

$$U_a = F_s 0.5 |S_{max} - S_{min}|, \tag{A.4}$$

where S_{max} is the maximum solution and S_{min} is the minimum solution of the three meshes (fine, medium, and coarse). Finally, results from the discretization study are analyzed using the relative discretization uncertainty U, defined as:

$$U = 100 \frac{U_a}{F_d}, \tag{A.5}$$

where F_d is the design grid. In this case, we take the medium grid $M2a$ as the design grid.

Following Table A.3, R_D shows monotone convergence for the examined parameter F^m ($R_D = 0.179$), with a resulting relative grid uncertainty of $U = 19.17\%$, which shows a satisfactory level of convergence. Cell resolution from the medium mesh $M2a$ (Table A.1) will be used in all test cases in this work, as it combines accuracy and computational cost more efficiently than the other two discretizations ($M1a$ and $M3a$).

Table B.4
Numerical grids used in the mesh sensibility analysis.

Mesh name	Discretization	Number of cells
Mesh1 ($M1b$)	$dx = 0.012$ m, $dy = 0.012$ m, $dz = 0.016$ m	0.6M
Mesh2 ($M2b$)	$dx = 0.006$ m, $dy = 0.006$ m, $dz = 0.008$ m	2.6M
Mesh3 ($M3b$)	$dx = 0.003$ m, $dy = 0.003$ m, $dz = 0.004$ m	6.4M

Table B.5
Relative discretization uncertainty, U[%].

Parameter	$M1b$	$M2b$	$M3b$	U[%]
P^m [Pa]	2153	3274	3285	13.6

Appendix B. Grid analysis 2: Dam-break interaction of a fluid impact on a vertical cylinder

Three grids, $M1b$ (coarse mesh), $M2b$ (medium mesh) and $M3b$ (fine mesh) (Table B.4), are used to establish the total uncertainty arising from temporal and spatial discretization errors.

The maximum pressure exerted (P^m) in the cylinder is used as the significant quantity for each grid size.

Following Table B.5, R_D shows monotone convergence for the examined parameter P^m ($R_D = 0.01$), with a resulting relative grid uncertainty of $U_a = 13.6\%$, which shows a satisfactory level of convergence. Cell resolution from the medium mesh $M2b$ (Table B.4) will be used.

Appendix C. Grid analysis 3: forces on a slender cylinder

A preliminary grid refinement study is carried out, following the approach described in Roache (1997), Stern et al. (2001) and Vukčević (2016). Three grids, $M1c$ (coarse mesh), $M2c$ (medium mesh) and $M3c$ (fine mesh) (Table C.6), are used to establish the total uncertainty arising from temporal and spatial discretization errors (Fig. C.20).

$M3c$ differs from $M2c$ in the vicinity of impermeable structures (ramp and cylinder) and in the free surface, where a refinement has been added to make the cell sizes half of their original size (Table C.6). A LES turbulence model, Smagorinsky (1963), has been selected because of its ability to resolve large flow structures resulting from the interaction of the granular landslide with a non-movable or deformable cylinder. The coefficient values for the Smagorinsky turbulence model are: $C_k = 0.094$; $C_e = 1.048$;

The maximum force exerted (F^m) in the cylinder is used as the significant quantity for each grid size. Following (Table C.7), R_D proves monotone convergence for both the examined parameters ($R_D = 0.10$), with a resulting relative grid uncertainty of $U_a = 5.88\%$, which shows a satisfactory level of convergence. Cell resolution from the medium mesh $M2c$

The maximum y + values around the ramp and the cylinder are less than 30 for the 3 simulations. The Pope (2000) criterion of the

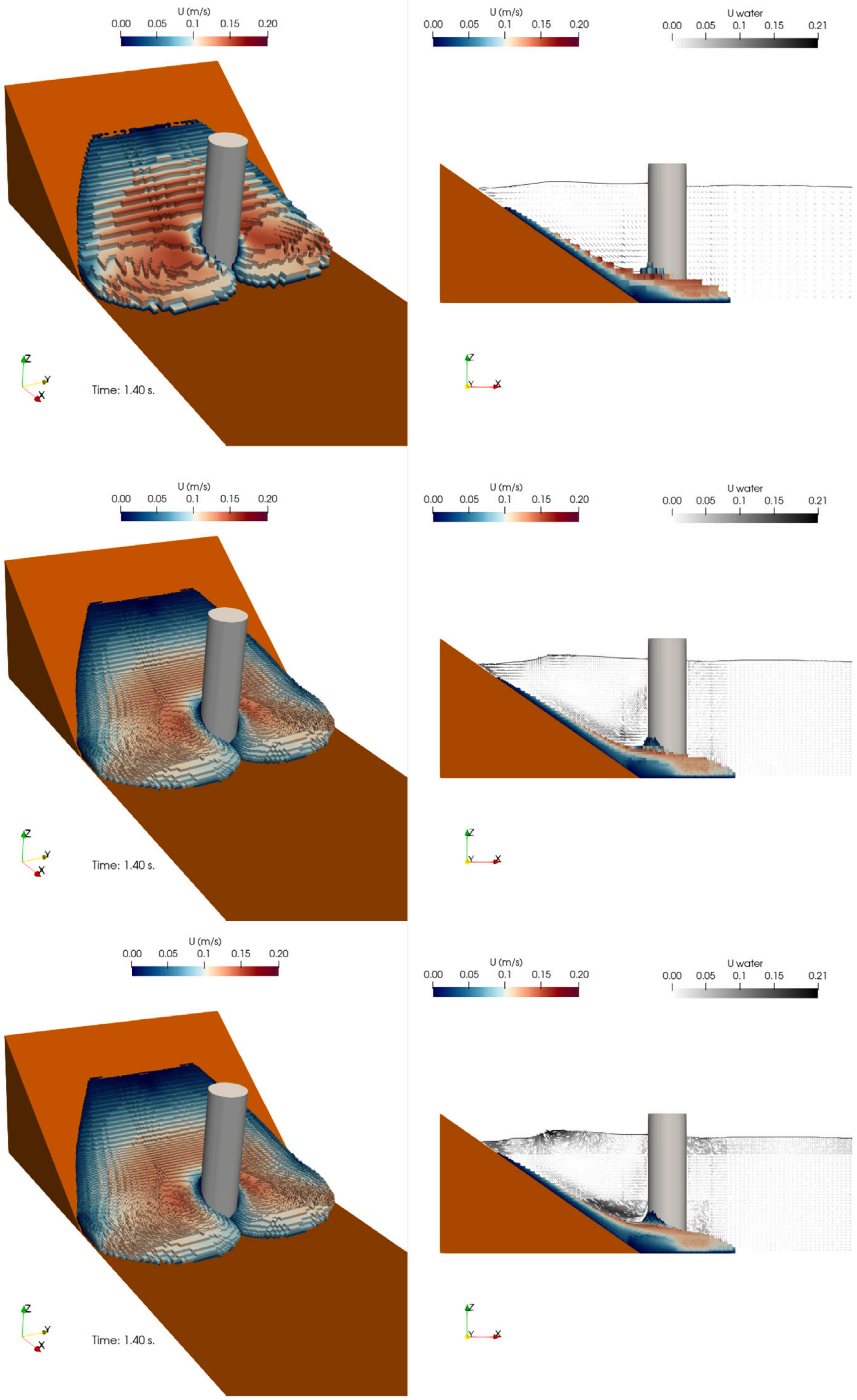

Fig. C.22. Left panels are a 3D plot of the velocity of the granular material and right panels are 2D views (plane XZ, y = 0.0.0 m) of the velocity of the granular material (blue-red) and the velocity of the water (white-black), plane XZ (y = 0.0 m). Top panel, mesh M1 (coarse), medium panel, mesh M2 (medium) and bottom panel, mesh M3 (fine), from Table C.6.

Table C.6
Numerical grids used in the mesh sensibility analysis.

Mesh name	Discretization	Cells
Mesh1 ($M1c$)	$dx = 0.012$ m, $dy = 0.012$ m, $dz = 0.016$ m	0.3M
Mesh2 ($M2c$)	$dx = 0.006$ m, $dy = 0.006$ m, $dz = 0.008$ m	2.3M
Mesh3 ($M3c$)	$dx = 0.006–0.003$ m, $dy = 0.006–0.003$ m, $dz = 0.008–0.004$ m	6.1M

Table C.7
Relative discretization uncertainty, U[%].

Parameter	$M1b$	$M2b$	$M3b$	U [%]
F^m [N]	20.9	23.9	24.3	5.88

quality of the LES simulation (M) for water is above 0.8 in the vicinity of the cylinder, in the ramp and in the interface granular material-water. The final numerical mesh $M1$ (0.3M cells) was run in serial in 1 processor, taking 1.5 days to numerically simulate 1.2 s. The final numerical mesh $M2$ (2.3M cells) was partitioned to run in parallel in 8 processors, taking 2.5 days to numerically simulate 1.2 s. The final numerical mesh $M3$ (6.1M cells) was partitioned to run in parallel in 16 processors, taking 2.5 days to numerically simulate 1.2 s.

Figs. C.20 depict the cell size discretization for mesh $M1c$ (coarse), mesh $M2c$ (medium) and mesh $M3c$ (fine). The left panels are top views and the right panels are side views (Plane XZ, y = 0.0 m). Fig. C.21 depicts the evolution of force over time for three meshes used in the grid analysis, $M1c$(black continuous line), $M2c$(red continuous line) and $M3c$(blue continuous line). Fig. C.22 presents a 3D plot of the velocity of the granular material (left panels) and 2D views (plane XZ, y = 0.0.0 m) of the velocity of the granular material (blue-red) and the velocity of the water (white-black), right panels (plane XZ, y = 0.0 m), for mesh $M1c$ (coarse), mesh $M2c$ (medium) and mesh $M3c$ (fine). It is observed that all three meshes reproduce the same hydrodynamic patterns around the structure. Furthermore, in medium and fine meshes, velocities of the water around the cylinder and below the generated wave are of the same order of magnitude.

References

Albaba, A., Lambert, S., Kneib, F., Chareyre, B., Nicot, F., 2017. DEM modeling of a flexible barrier impacted by a dry granular flow. Rock Mech. Rock Eng. 50 (11), 3029–3048, Springer.

Chauchat, J., Cheng, Z., Nagel, T., Bonamy, C., Hsu, T.-J., 2017. SedFoam-2.0: a 3-D two-phase flow numerical model for sediment transport. Geosci. Model. Dev. 10 (12), 4367–4392, Copernicus GmbH.

Cui, L., Jeng, D.-S., 2024. Two-dimensional one-way coupled modelling for fluid–structure-seabed interactions around a semicircular breakwater using OpenFOAM. Appl. Ocean Res. 153, 104249.

Cuomo, S., 2021. MPM modelling of buildings impacted by landslides. In: Understanding and Reducing Landslide Disaster Risk: Volume 5 Catastrophic Landslides and Frontiers of Landslide Science. Springer International Publishing, Cham, pp. pp. 245–266.

Da Cruz, F., Emam, S., Prochnow, M., Roux, J.-N., Chevoir, F., 2005. Rheophysics of dense granular materials: Discrete simulation of plane shear flows. Phys. Rev. E—Statistical, Nonlinear Soft Matter Phys. 72 (2), 021309, APS.

Di Paolo, B., Lara, J.L., Barajas, G., Losada, I.J., 2021a. Wave and structure interaction using multi-domain couplings for Navier–Stokes solvers in OpenFOAM®. Part I: Implementation and validation. Coast. Eng. 164, 103799.

Di Paolo, B., Lara, J.L., Barajas, G., Losada, I.J., 2021b. Waves and structure interaction using multi-domain couplings for Navier–Stokes solvers in openfoam®. Part II: Validation and application to complex cases. Coast. Eng. 164, 103818.

Domnik, B., Pudasaini, S.P., 2012. Full two-dimensional rapid chute flows of simple viscoplastic granular materials with a pressure-dependent dynamic slip-velocity and their numerical simulations. J. Non-Newton. Fluid Mech. 173, 72–86, Elsevier.

Ekat, A.-K., Weissenbrunner, A., Straka, M., Eichler, T., Oberleithner, K., 2023. Hybrid LES/RANS simulations of a 90° pipe bend using different CFD solvers. OpenFOAM®J. 3, 49–65, OpenCFD Ltd, Bracknell, U.K.

ESI-Group, 2023. Openfoam the open source CFD toolbox. Available at: https://www.openfoam.com/.

Fall, A., Ovarlez, G., Hautemayou, D., Mézière, C., Roux, J.-N., Chevoir, F., 2015. Dry granular flows: Rheological measurements of the μ(I)-rheology. J. Rheol. 59 (4), 1065–1080, AIP Publishing.

Fan, N., Zhang, W., Sahdi, F., Nian, T., 2022. Evaluation of horizontal submarine slide impact force on pipeline via a modified hybrid geotechnical–fluid dynamics framework. Can. Geotech. J. 59 (6), 827–836.

Fang, J., Wang, L., Hong, Y., Zhao, J., 2022. Influence of solid–fluid interaction on impact dynamics against rigid barrier: CFD–DEM modelling. Géotechnique 72 (5), 391–406, Thomas Telford Ltd.

Gauer, P., Elverhoi, A., Issler, D., De Blasio, F.V., 2006. On numerical simulations of subaqueous slides: back-calculations of laboratory experiments of clay-rich slides. Nor. Geol. Tidsskr. 86 (3), 295, Scandinavian University Press.

Gilletta, A., Bonamy, C., Robert, M., Chauchat, J., 2025. Assessment of hybrid RANS/LES models for the prediction of the flow and scour around a wall-mounted cylinder. Adv. Water Resour. 199, 104934.

Grilli, S.T., Shelby, M., Kimmoun, O., et al., 2017. Modeling coastal tsunami hazard from submarine mass failures: effect of slide rheology, experimental validation, and case studies off the US East Coast. Nat. Hazards 104391.

Guo, X.-s., Nian, T.-k., Fan, N., Jia, Y.-g., 2021. Optimization design of a honeycomb-hole submarine pipeline under a hydrodynamic landslide impact. Mar. Georesources Geotechnol. 39 (9), 1055–1070, Taylor & Francis.

Jasak, H., 1996. Error Analysis and Estimation for the Finite Volume Method with Applications To Fluid Flows (Ph.D thesis). Imperial College London (University of London). Imperial College London (University of London).

Jiang, Y.-J., Towhata, I., 2013. Experimental study of dry granular flow and impact behavior against a rigid retaining wall. Rock Mech. Rock Eng. 46 (4), 713–729, Springer.

Jop, P., Forterre, Y., Pouliquen, O., 2005. Crucial role of sidewalls in granular surface flows: consequences for the rheology. J. Fluid Mech. 541, 167–192, Cambridge University Press.

Kaiser, M.J., 2017. U.S. gulf of Mexico deepwater pipeline construction – a review of lessons learned. Mar. Policy 86, 214–233.

Kamra, M.M., Salami, J.Al., Sueyoshi, M., Hu, C., 2019. Experimental study of the interaction of dambreak with a vertical cylinder. J. Fluids Struct. 86, 185–199.

Larsen, B.E., Fuhrman, D.R., 2018. On the over-production of turbulence beneath surface waves in Reynolds-averaged Navier–Stokes models. J. Fluid Mech. 853, 419–460, Cambridge University Press.

Launder, B.E., Sharma, B.I., 1974. Application of the energy-dissipation model of turbulence to the calculation of flow near a spinning disc. Lett. Heat Mass Transfer 1 (2), 131–137.

Leonardi, A., Wittel, F.K., Mendoza, M., Vetter, R., Herrmann, H.J., 2016. Particle–fluid–structure interaction for debris flow impact on flexible barriers. Computer-Aided Civ. Infrastruct. Eng. 31 (5), 323–333, Wiley Online Library.

Li, Y., Fuhrman, D.R., 2022. On the turbulence modelling of waves breaking on a vertical pile. J. Fluid Mech. 953, Cambridge University Press.

Li, X., Zhao, J., 2018. A unified CFD-DEM approach for modeling of debris flow impacts on flexible barriers. Int. J. Numer. Anal. Methods Geomech. 42 (14), 1643–1670, Wiley Online Library.

Liu, C., Liang, L., 2022. A coupled SPH–DEM–FEM approach for modeling of debris flow impacts on flexible barriers. Arab. J. Geosci. 15 (5), 420, Springer.

Liu, J., Tian, J., Yi, P., 2015. Impact forces of submarine landslides on offshore pipelines. Ocean Eng. 95, 116–127.

Luna, B.Quan., Blahut, J., van Westen, C.J., Sterlacchini, S., van Asch, T.W.J., Akbas, S.O., 2011. The application of numerical debris flow modelling for the generation of physical vulnerability curves. Nat. Hazards Earth Syst. Sci. 11 (7), 2047–2060.

Luo, H.Y., Shen, P., Zhang, L.M., 2019. How does a cluster of buildings affect landslide mobility: a case study of the shenzhen landslide. Landslides..

Luo, H.Y., Zhang, L.M., Zhang, L.L., He, J., Yin, K.S., 2023. Vulnerability of buildings to landslides: The state of the art and future needs. Earth-Sci. Rev. 238, 104329.

Luo, G., Zhao, Y., Shen, W., Wu, M., 2022. Dynamics of bouldery debris flow impacting onto rigid barrier by a coupled SPH-DEM-FEM method. Comput. Geotech. 150, 104936, Elsevier.

Martin, G.R., Chen, C.-Y., 2005. Response of piles due to lateral slope movement. Comput. Struct. 83 (8), 588–598.

Menter, F., 1993. Zonal two equation k-w turbulence models for aerodynamic flows. In: 23rd Fluid Dynamics, Plasmadynamics, and Lasers Conference.

Mohammed, F., Fritz, H.M., 2012. Physical modeling of tsunamis generated by three-dimensional deformable granular landslides. J. Geophys. Res.: Ocean. 117 (C11), Wiley Online Library.

Montellà, E.P., Chauchat, J., Bonamy, C., Weij, D., Keetels, G.H., Hsu, T.-J., 2023. Numerical investigation of mode failures in submerged granular columns. Flow 3, E28, Cambridge University Press.

Montellà, E.P., Chauchat, J., Chareyre, B., Bonamy, C., Hsu, T.-J., 2021. A two-fluid model for immersed granular avalanches with dilatancy effects. J. Fluid Mech. 925, A13, Cambridge University Press.

Paris, A., Heinrich, P., Abadie, S., 2021. Landslide tsunamis: Comparison between depth-averaged and Navier–Stokes models. Coast. Eng. 170, 104022.

Pope, S.B., 2000. Turbulent Flows. Cambridge University Press, Cambridge.

Qian, X., Liu, Z., Xu, J., 2023. New insights into quantifying the stable impact forces of a submarine debris flow on a pipeline. Ocean Eng. 274, 114060.

Qian, X., Xu, J., Bai, Y., Das, H.S., 2020. Formation and estimation of peak impact force on suspended pipelines due to submarine debris flow. Ocean Eng. 195, 106695.

Qwist, J.R.K., Christensen, E.D., 2023. Development and implementation of a direct surface description method for free surface flows in OpenFOAM. Coast. Eng. 179, 104227.

Rauter, M., 2021. The compressible granular collapse in a fluid as a continuum: validity of a Navier–Stokes model with-I-rheology. J. Fluid Mech. 915 (A87), Cambridge University Press.

Rauter, M., Hoße, L., Mulligan, R.P., Take, W.A., Lø vholt, F., 2021. Numerical simulation of impulse wave generation by idealized landslides with openfoam. Coast. Eng. 165, 103815.

Rauter, M., Viroulet, S., Gylfadóttir, S.S., Fellin, W., Løvholt, F., 2022a. Granular porous landslide tsunami modelling – the 2014 Lake Askja flank collapse. Nat. Commun..

Ren, Z., Zhao, X., Liu, H., 2019. Numerical study of the landslide tsunami in the south China sea using Herschel-Bulkley rheological theory. Phys. Fluids 31 (5), AIP Publishing.

Renaud, M., Bertrand, O., Bonamy, C., Chauchat, J., 2025. SedExnerFoam 2412: A 3D exner-based sediment transport and morphodynamics model. EGUsphere 2025, 1–36.

Roache, P., 1997. Quantification of uncertainty in computational fluid dynamics. Ann. Rev. Fluid Mech 29, 123–160.

Rodi, W., Constantinescu, G., Stoesser, T., 2013. Large-eddy simulation in hydraulics, first ed. In: IAHR monograph.

Romano, A., Bellotti, G., Barajas, G., Lara, J.L., 2025. On the energy transfer of tsunamis generated by subaerial granular landslides: A 2D numerical analysis. Coast. Eng. 104821.

Romano, A., Lara, J.L., Barajas, G., Di Paolo, B., Bellotti, G., Di Risio, M., Losada, I.J., 2020. Tsunamis generated by submerged landslides: Numerical analysis of the near-field wave characteristics. J. Geophys. Res.: Ocean. 125 (7), e2020JC016157.

Romano, A., Lara, J.L., Barajas, G., Losada, I.J., 2023. Numerical modeling of tsunamis generated by granular landslides in openfoam®: A Coulomb viscoplastic rheology. Coast. Eng. 186, 104391.

Salim, S., Pattiaratchi, C., Tinoco, R., Coco, G., Hetzel, Y., Wijeratne, S., Jayaratne, R., 2017. The influence of turbulent bursting on sediment resuspension under unidirectional currents. Earth Surf. Dyn. 5 (3), 399–415.

Schumann, U., 1996. Direct and large eddy simulations of stratified homogeneous shear flows. Dyn. Atmos. Oceans 23 (1), 81–98.

Smagorinsky, J., 1963. GENERAL circulation experiments WITH the PRIMITIVE equations: I. the BASIC experiment. Mon. Weather Rev. 91 (3), 99–164, American Meteorological Society.

Spalart, P., Shur, M., Strelets, M., Travin, A., 2012. Sensitivity of landing-gear noise predictions by large-eddy simulation to numerics and resolution. In: 50th AIAA Aerospace Sciences Meeting Including the New Horizons Forum and Aerospace Exposition.

Stern, F., Wilson, R., Coleman, H., Paterson, E., 2001. Comprehensive approach to verification and validation of CFD simulations—Part 1: Methodology and procedures. J. Fluids Eng 123, 793–802.

T.-k., Nian, Guo, X.-s., Fan, N., Jiao, H.-b., Li, D.-y., 2018. Impact forces of submarine landslides on suspended pipelines considering the low-temperature environment. Appl. Ocean Res. 81, 116–125.

Viroulet, S., Sauret, A., Kimmoun, O., 2014. Tsunami generated by a granular collapse down a rough inclined plane. Europhys. Lett. 105 (3), 34004, IOP Publishing.

Von Boetticher, A., Turowski, J.M., McArdell, B.W., Rickenmann, D., Kirchner, J.W., 2016. DebrisInterMixing-2.3: A finite volume solver for three-dimensional debris-flow simulations with two calibration parameters - part 1: Model description. Geosci. Model. Dev. 9 (9), 2909–2923.

Vukčević, V., 2016. Numerical Modelling of Coupled Potential and Viscous Flow for Marine Applications (Ph.D thesis). University of Zagreb.

Wang, Z., Zheng, D., Guo, X., 2024. Investigation of offshore landslides impact on bucket foundations using a coupled SPH–FEM method. Geoenviron Disasters..

Wilcox, D.C., 1988. Reassessment of the scale-determining equation for advanced turbulence models. AIAA J. 26 (11), 1299–1310.

Wilcox, D.C., 2006. Turbulence Modeling for CFD, vol. 1, DCW Industries.

Zakeri, A., Hø eg, K., Nadim, F., 2008. Submarine debris flow impact on pipelines — Part I: Experimental investigation. Coast. Eng. 55 (12), 1209–1218.

Zhang, B., Huang, Y., Lu, P., Li, C., 2020. Numerical investigation of multiple-impact behavior of granular flow on a rigid barrier. Water 12 (11), 3228, MDPI.

Zhong, H., Yu, Z., Zhang, C., Lyu, L., Zhao, L., 2022. Dynamic mechanical responses of reinforced concrete pier to debris avalanche impact based on the DEM-FEM coupled method. Int. J. Impact Eng. 167, 104282.